

Bayesian Inference for Brain Activity from Functional Magnetic Resonance Imaging Collected at Two Spatial Resolutions

Andrew S. Whiteman¹, Andreas J. Bartsch² Jian Kang¹ and Timothy D. Johnson¹

¹*Department of Biostatistics, University of Michigan School of Public Health, e-mail: awhitem@umich.edu e-mail: jiankang@umich.edu e-mail: tdjtdj@umich.edu*

²*Radiologie Bamberg and Department of Neuroradiology, University of Heidelberg, e-mail: dr.bartsch@radiologie-bamberg.de*

Abstract: Neuroradiologists and neurosurgeons increasingly opt to use functional magnetic resonance imaging (fMRI) to map functionally relevant brain regions for noninvasive presurgical planning and intraoperative neuronavigation. This application requires a high degree of spatial accuracy, but the fMRI signal-to-noise ratio (SNR) decreases as spatial resolution increases. In practice, fMRI scans can be collected at multiple spatial resolutions, and it is of interest to make more accurate inference on brain activity by combining data with different resolutions. To this end, we develop a new Bayesian model to leverage both better anatomical precision in high resolution fMRI and higher SNR in standard resolution fMRI. We assign a Gaussian process prior to the mean intensity function and develop an efficient, scalable posterior computation algorithm to integrate both sources of data. We draw posterior samples using an algorithm analogous to Riemann manifold Hamiltonian Monte Carlo in an expanded parameter space. We illustrate our method in analysis of presurgical fMRI data, and show in simulation that it infers the mean intensity more accurately than alternatives that use either the high or standard resolution fMRI data alone.

Keywords and phrases: Imaging statistics, Gaussian process, Bayesian nonparametrics, Data integration, Presurgical fMRI.

1. Introduction

Neurosurgery presents a unique set of challenges to the operating surgeon. Treatment of brain tumors, for example, is handled primarily by surgical resection when possible. Gliomas are often infiltrative, however, and as a result may be impossible to remove entirely (Jovčevska, Kočevar and Komel, 2013; Stippich, 2015). The neurosurgeon’s goal is typically to resect as much of the tumor as possible while avoiding damage to surrounding healthy areas of brain tissue, requiring precise structural and functional information. Although the structure of the human brain shares a gross organization common across individuals, functional neuroanatomy may vary between patients and within regions (e.g. Large et al., 2016), highlighting the need for within-patient precision. Here we propose a model that leverages the massive amount of spatial data available in individual functional magnetic resonance imaging (fMRI) scans to help guide presurgical planning by identifying functionally relevant brain regions in a patient-specific manner.

Traditionally, electrocortical interference is used to map brain functional organization during surgery (e.g. Cordella et al., 2013), but this procedure is highly invasive, lengthens surgery duration, and cannot be incorporated into presurgical planning (Stippich, 2015). Clinicians can also opt to use imaging methods to help inform patient-specific presurgical planning and intraoperative neuronavigation (e.g. Archip et al., 2007; Nimsky et al., 2006; Durnez et al., 2013; Silva et al., 2018). fMRI may be used, for example, to map patient-specific functional areas, but the data come with an inherent trade off. Surgeons would like to collect information that is spatially precise, but the fMRI signal-to-noise ratio (SNR) decreases as spatial resolution increases, potentially making functional mapping more difficult (Bodurka et al., 2007). In practice, modern scanners are equipped

to handle a variety of image resolutions by modifying magnetic pulse sequences, so radiologists are in principle able to collect any combination of scans advantageous for presurgical planning.

Our motivating datasets come from two separate fMRI experiments in which preoperative patients performed cognitive tasks chosen to localize brain regions involved in language processing (see sections 2 and 4 for details). Each individual patient was administered their task over two separate scanning runs, collected at different spatial resolutions. Details vary by patient, but in both instances one run was collected at “standard” spatial resolution with voxel (volumetric pixel) dimensions measuring approximately $3 \times 3 \times 3 \text{ mm}^3$, and the other was collected at “high” spatial resolution with approximately $2 \times 2 \times 2 \text{ mm}^3$ voxels. Raw image time series data were preprocessed using standard software (Jenkinson et al., 2012; Woolrich et al., 2001) to yield statistical parametric maps for each spatial resolution that summarized patients’ fMRI activation over time. In this paper, we propose a new Bayesian model to integrate both sources of data, leveraging the anatomical/spatial precision of high resolution fMRI and the SNR of standard resolution fMRI for enhanced within-patient precision. The primary goal of our model is to reduce spatial noise while making inferential statements identifying functional regions at the highest resolution available. Conceptually, we accomplish this goal by modeling the mean intensity function of both data sources as a Gaussian process. Gaussian processes induce a probability measure on a functional space with distribution characterized by a mean and covariance function (Rasmussen and Williams, 2006). Conditional on the covariance function hyperparameters, which we estimate from data, we conduct fully Bayesian inference on the mean function measured at voxel locations in the high spatial resolution image.

In addition to spatial precision, computational complexity is also a major concern since excessive latency between preoperative scanning and a patient’s actual surgery is undesirable. Computation with spatial Gaussian process models typically involve decomposition of an $n \times n$ matrix, where n is the number of spatial locations. Between the two image types there are over 200,000 unique spatial locations in each of our motivating datasets, rendering usual computational approaches to inference intractable in most computing environments. Here, we outline a modification of the typical Hamiltonian Monte Carlo (HMC) algorithm that makes this inference not only feasible but computationally efficient. To do so, we propose a dual resolution mapping prior that generalizes the existing Gaussian predictive process framework (e.g. Seeger, Williams and Lawrence, 2003; Banerjee et al., 2008) to our setting with multiple data sources. Our algorithm further harnesses a parameter expansion idea from Wood and Chan (1994) to sample from the posterior using Riemann manifold Hamiltonian dynamics (Girolami and Calderhead, 2011) in an ultrahigh dimensional parameter space.

Our model is related to existing literature from the field of spatial statistics that consider the “change of support problem” (e.g. Gelfand, Zhu and Carlin, 2001; Fuentes and Raftery, 2005; Berrocal, Gelfand and Holland, 2012). Such models have been used, for example, to combine data from air pollution monitoring sites with simulations from physical models for prediction at unobserved locations and model validation. Studies such as these commonly model conditional relationships between data sources, for example by regressing measured air pollution onto physical model output. Our multi-resolution imaging paradigm is related in the sense that we would like to use standard resolution data to improve inference in high resolution space. This goal, however, is complicated by the fact that high and standard spatial resolution voxels in general only partially overlap with their neighbors in their complementary image (see Fig. 1). We will, however, take a different approach by modeling both sources of data as joint outcomes. Not only does this approach perhaps make more conceptual sense for modeling multiple image types, it permits flexible and natural reconfiguration in response to real world challenges. For example, if only one fMRI resolution or session is available presurgically, the missing data can be removed from the joint outcome. Though we discuss our method exclusively in a functional neuroimaging context, the method can easily generalize to other imaging modalities or indeed to spatial data with mixed supports more broadly.

Whereas the inferential goal of most neuroimaging studies is to identify activated or deactivated brain regions while controlling the family-wise error rate, we take a somewhat different approach

given specific presurgical needs. In a neurosurgical context, clinicians are typically more concerned with inaccurate labeling of functionally important tissue as unimportant. To this end, we adopt a decision theoretic rule from previous work to control the ratio of false negative to false positive errors (Liu et al., 2016, 2019; Müller, Parmigiani and Rice, 2006). We show in simulation that our dual resolution method achieves good accuracy for realistic effect sizes. Specifically, our method outperformed single spatial resolution alternatives in terms of both false negative and false positive error rates when the number of discoveries was fixed across methods. Software to fit the dual and single resolution models discussed in this paper to data stored in the NIFTI data standard (Cox et al., 2004) is available online (Whiteman, 2022).

The body of this paper contains descriptions of our motivating clinical datasets in section 2, and a summary of the method we propose to handle the unique challenges of those data in section 2.1. In sections 2.2 and 2.3, we elaborate on our approach to enable precise estimation and computation in such a large parameter space. We discuss a strategy to conduct inference based on weighted trade offs between false negative and false positive errors in section 2.4. We quantify our method’s performance against single resolution alternative methods in section 3. Section 4 reports on analyses of real patient data using our proposed method for dual resolution fMRI. Finally, we present an overall evaluation of our contributions in section 5.

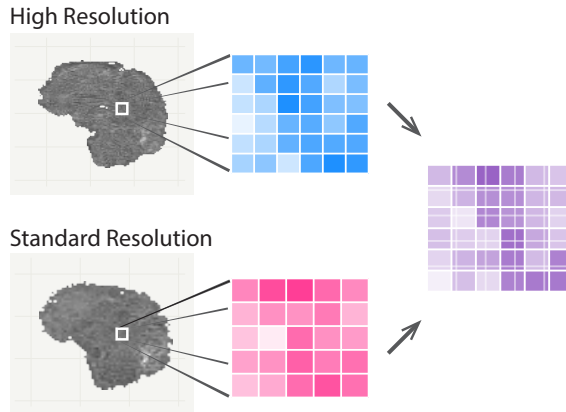


Fig 1: Schematic of aims and difficulties with integration of fMRI data collected at multiple spatial resolutions. Images collected at different resolutions exhibit inherently different levels of noise. We would like to reduce spatial noise while making inferential statements at the highest resolution available, but voxel locations may not align in general. See the online version for color figures.

2. Data and methods

We developed the method presented here to analyze single-patient presurgical fMRI data collected at two spatial resolutions. Our first motivating dataset comes from a 62 year old right handed woman—“patient 1”—who presented difficulties with reading, finding, and comprehending words. This patient was subsequently found to have a tumor in her left middle and inferior temporal gyrus. Prior to surgery, the patient was scanned while performing a reading task to map brain areas associated with reading non-final embedded clause sentences and language processing. Scans were collected in two separate runs: once at standard $3 \times 3 \times 3.45 \text{ mm}^3$ resolution ($64 \times 64 \times 48$ grid), and once at high $1.8 \times 1.8 \times 2.3 \text{ mm}^3$ resolution ($120 \times 120 \times 62$ grid).

Our second motivating dataset comes from an 18 year old right handed woman—“patient 2”—who presented after a general seizure and was subsequently found to have a cavernoma in her left

temporal lobe (see Appendix B for more detail). For cavernomas in critical areas, presurgical fMRI is considered one option—as with brain tumors—to map brain function noninvasively for presurgical planning and intraoperative neuronavigation. Patient 2 was also scanned prior to surgery while performing a language processing task. Her standard resolution data were collected with slightly smaller $3 \times 3 \times 3.3 \text{ mm}^3$ voxels ($64 \times 64 \times 48$ grid), and her high resolution data with $1.8 \times 1.8 \times 2.2 \text{ mm}^3$ voxels ($120 \times 120 \times 62$ grid). As in this patient, cavernomas typically cause profound T2*-weighted MR signal loss, with blooming into surrounding brain tissue. Signal loss is caused by abrupt differences in magnetic susceptibility in apposed tissues and is a common occurrence in clinical fMRI (e.g. intratumoral hemorrhages can cause similar dropout). We use this patient’s data to illustrate our model’s capacity to recover an estimate of activation in areas of such fMRI signal loss.

fMRI time series preprocessing without spatial smoothing was performed prior to our analysis using FSL software (Jenkinson et al., 2012) and the FEAT tool (Woolrich et al., 2001). As will become clear in section 2.1, our model imposes smoothness on the image mean function, and so we avoided smoothing the data during preprocessing (beyond the small amount of unavoidable smoothing that can occur when time series images from the two spatial resolutions are motion corrected and co-registered with one another). Smoothing is an otherwise ubiquitous step in typical fMRI pipelines, but over smoothing is not desirable for presurgical planning applications as it may reduce spatial precision by, for example, smearing activation into adjacent areas when the smoothing kernel is too wide. Data were corrected for motion and temporally high pass filtered, and marginal linear models were fit to the time series data at each voxel to create summary statistic maps of task-related activation.

Preprocessing resulted in one unsmoothed z -statistic contrast image for each fMRI resolution that summarized task-related activation over the course of each respective scan. We went on to use the generated test statistic maps as outcome data in our subsequent analysis, treating the images as noisy measures of true activation. Although we may find it beneficial to include both spatial and temporal data in our modeling framework in future work, the present model only explicitly represents a spatial process. As such, throughout the rest of this paper we will use “high resolution,” for example, as a stand in for “high *spatial* resolution” etc. In the greater imaging community, however, “resolution” could in general relate to frequency of either spatial or temporal data collection, or both. We give additional details regarding patient data collection and image preprocessing in Appendix A.

2.1. Bayesian dual resolution mapping

Let \mathcal{B} denote a generic brain image space, and let $B_h \subset \mathcal{B}$ and $B_s \subset \mathcal{B}$ denote the sets of spatial locations in the brain where high and standard resolution functional MRI data are collected, respectively. For reference, the number of voxels $|B_h| \approx 200,000$ in the high resolution image, and $|B_s| \approx 50,000$ in the standard resolution image. Each atom $\mathbf{v} \in \mathcal{B}$ is a three dimensional vector of spatial coordinates relative to some origin point $\mathbf{v}_0 \in \mathcal{B}$; the Euclidean distance between any two points, $\mathbf{v}, \mathbf{v}' \in \mathcal{B}$ can be represented $\|\mathbf{v} - \mathbf{v}'\|_2$, and is typically measured in millimeters. Although data at a given voxel is associated with a small volume, we follow common practice and essentially treat that data as observed on location \mathbf{v} exactly. In general, even voxels that overlap between the two image types may not have the same centers, so that the set of points in the intersection $B_h \cap B_s$ may be empty.

Conceptually, we motivate our proposed model as follows. Let $Y_h(\mathbf{v}_h)$ denote the high resolution imaging outcome at voxel \mathbf{v}_h , and let $Y_s(\mathbf{v}_s)$ denote the standard resolution imaging outcome at voxel \mathbf{v}_s . For the same patient performing the same cognitive task in the same scanner, we make the assumption that $Y_h(\mathbf{v}_h)$ and $Y_s(\mathbf{v}_s)$ are realizations from a unifying generative process. Let $\mathcal{N}(\mu, \sigma^2)$ denote a Gaussian distribution with mean μ and variance σ^2 . We model the data as

jointly Gaussian,

$$\begin{aligned} Y_h(\mathbf{v}_h) &\sim \mathcal{N}(\mu(\mathbf{v}_h), \sigma_h^2), & \mathbf{v}_h &\in B_h \\ Y_s(\mathbf{v}_s) &\sim \mathcal{N}(\mu(\mathbf{v}_s), \sigma_s^2), & \mathbf{v}_s &\in B_s \end{aligned} \quad (1)$$

where $\mu(\mathbf{v})$ represents the expected intensity of brain activity in voxel $\mathbf{v} \in \mathcal{B}$, and σ_h^2 and σ_s^2 are noise variances in the high and standard resolution images, respectively. Because our data were not smoothed, we modeled noise as a spatially independent and additive process. Given the known phenomenon that SNR increases with voxel volume (e.g. [Bodurka et al., 2007](#)), we expect standard resolution images to be less noisy than high resolution images. We therefore adopted a weakly informative prior for the noise variances with the restriction $\sigma_h^2 > \sigma_s^2$:

$$\pi(\sigma_h^2, \sigma_s^2) \propto \sigma_h^{-2} \sigma_s^{-2} \mathbb{1}(0 < \sigma_s^2 < \sigma_h^2), \quad (2)$$

where $\mathbb{1}(\cdot) \in \{0, 1\}$ is the event indicator function ($\mathbb{1}(\mathcal{A}) = 1$ if \mathcal{A} occurs, and 0 otherwise).

For functional maps, we are primarily interested in making inferences about the mean intensity function, $\mu(\cdot)$, to which we assign a mean zero Gaussian process prior,

$$\mu(\mathbf{v}) \sim \mathcal{GP}(0, K(\mathbf{v}, \mathbf{v}')). \quad (3)$$

In our formulation, the function $\mu(\cdot)$ captures all of the correlation between voxels and between the two images; conditional on $\mu(\cdot)$, $Y_h(\mathbf{v}_h)$ and $Y_s(\mathbf{v}_s)$ are mutually independent across all $\mathbf{v}_h \in B_h$ and $\mathbf{v}_s \in B_s$. We implicitly assume that the two brain images share a real-world coordinate system, and that $\mu(\mathbf{v})$ is correlated with $\mu(\mathbf{v}')$ if the distance $\|\mathbf{v} - \mathbf{v}'\|_2$ is small. A variety of preprocessing techniques have been developed to align 3D images and ensure the former assumption holds with minimal error (e.g. [Reuter, Rosas and Fischl, 2010](#); [Jenkinson et al., 2012](#)).

Since anatomical precision is paramount in our application, we would like to conduct inference on $\mu(\cdot)$ for all locations in B_h . To facilitate this goal while simultaneously modeling the cross correlation between $\mu(\cdot)$ evaluated on locations in B_h and B_s , we introduce a nonstationary covariance function to map between data sets. For any $\mathbf{v}, \mathbf{v}' \in \mathcal{B}$, let,

$$K(\mathbf{v}, \mathbf{v}') = \begin{cases} k(\mathbf{v}, \mathbf{v}') & \text{if } \mathbf{v}' \in B_h \\ w^\top(\mathbf{v})k(B_h, \mathbf{v}') & \text{otherwise,} \end{cases} \quad (4)$$

where $w(\cdot)$ is a vector of weights in a finite basis (defined below; chosen so that the covariance function is symmetric for all $\mathbf{v}, \mathbf{v}' \in \mathcal{B}$), and $k(\cdot, \cdot)$ is some positive definite function with range $\mathbb{R}_{>0}$. In our application, we take $k(\cdot, \cdot)$ to be the isotropic radial basis function,

$$k(\mathbf{v}, \mathbf{v}') = \tau^2 \exp(-\psi \|\mathbf{v} - \mathbf{v}'\|_2^\nu), \quad \tau^2, \psi > 0, \quad \nu \in (0, 2], \quad (5)$$

and extend the notation to apply to sets of locations so that $k(B_h, \mathbf{v}') = [k(\mathbf{v}_h, \mathbf{v}')]_{\mathbf{v}_h \in B_h}$ is a vector in $\mathbb{R}^{|B_h|}$. In (5), $\tau^2 > 0$ is the ‘‘partial sill’’ or marginal prior variance of $\mu(\cdot)$, the decay parameter $\psi > 0$ defines the correlation bandwidth, and $\nu \in (0, 2]$ is the kernel exponent or smoothness parameter. We define the covariance parameters $\boldsymbol{\theta} = (\tau^2, \psi, \nu)^\top$; ψ and ν , are commonly fixed prior to analyses, but because of the abundance of spatial data in even a single brain image, in practice we recommend estimating these parameters from data (see section 4.1 for details). The custom kernel in (4) was designed to approximate a ‘‘Gaussian parent process’’ ([Banerjee et al., 2008](#)) with isotropic radial basis covariance (5) everywhere in \mathcal{B} . We arrange our presentation here to make clear that we use (4) directly, and obtain exact inference with the prior (3) specified in this way. A careful choice of the weight function $w(\cdot)$, moreover, can render the problem more computationally tractable.

2.2. Construction of the covariance weights

By the definition of a Gaussian process, $\mu(\mathbf{v})$ and $\mu(\mathbf{v}')$ are jointly multivariate Gaussian distributed for any distinct locations \mathbf{v} and \mathbf{v}' . As a result, Gaussian process models promote natural and flexible predictions of values of $\mu(\cdot)$ at unobserved locations. For arbitrary collections of locations $U = \{\mathbf{v}_1, \dots, \mathbf{v}_n\} \subset \mathcal{B}$ and $V = \{\mathbf{v}'_1, \dots, \mathbf{v}'_m\} \subset \mathcal{B}$, we define $\mu(U) = [\mu(\mathbf{v}_i)]_{i=1}^n$ as a vector in \mathbb{R}^n ; $K(U, \mathbf{v}) = [K(\mathbf{v}_i, \mathbf{v})]_{i=1}^n$ as a vector in \mathbb{R}^n ; and $K(U, V) = [K(\mathbf{v}_i, \mathbf{v}'_j)]_{i,j=1}^{n,m}$ as a matrix in $\mathbb{R}^{n \times m}$. If, for example, V is a set of observed locations, and U are unobserved locations, then conditional on $\mu(V)$, $\mu(U)$ is multivariate Gaussian distributed with mean $K(U, V)K(V, V)^{-1}\mu(V)$ and variance $K(U, U) - K(U, V)K(V, V)^{-1}K(V, U)$.

Since imaging data is collected on a dense grid we often have no need to predict outcomes at unobserved or non-brain locations, except in cases of signal loss or other artifact. We made use of the kriging or conditional distribution relationships above primarily to define the basis weight function $w(\cdot)$ to integrate information from both high and standard resolution images. We constructed the basis weights in (4) so that $w(\mathbf{v}) \approx K(B_h, B_h)^{-1}k(B_h, \mathbf{v})$, with the ‘‘approximate’’ relation explained below. This formulation allowed us to leverage the relationship that $w^\top(\mathbf{v})\boldsymbol{\mu}_h$ approximates the prior conditional expectation of $\mu(\mathbf{v})$ given $\boldsymbol{\mu}_h = \mu(B_h)$. As such, our construction in (4) generalizes a Gaussian predictive process framework (e.g. Seeger, Williams and Lawrence, 2003; Banerjee et al., 2008) to our setting with multiple data sources by using B_h as a high-dimensional reference set. In general, within this framework we could have defined the weights $w(\cdot)$ based on any arbitrary set of knot locations $B_* \subset \mathcal{B}$. Since inference at a fine spatial scale typically requires a dense set of knot locations (e.g. Stein et al., 2007), we preferred to define $w(\cdot)$ based on all of B_h .

Our covariance function in (4) effectively employs kriging methods to map $\mu(B_h)$ onto the locations in B_s so that the standard resolution data can still inform $\mu(B_h)$ in the posterior. Switching to vector notation, let $\boldsymbol{\mu}_s = \mu(B_s)$. We express the prior in (3),

$$\pi(\boldsymbol{\mu}_h, \boldsymbol{\mu}_s) = \mathcal{N}\left(\mathbf{0}, \begin{bmatrix} \mathbf{K}_h & \mathbf{K}_{h,s} \\ \mathbf{K}_{s,h} & \mathbf{K}_{s,h}\mathbf{K}_h^{-1}\mathbf{K}_{h,s} \end{bmatrix}\right). \quad (6)$$

where $\boldsymbol{\mu}_h$ and $\boldsymbol{\mu}_s$ are the means of the high, and standard resolution images, respectively; we denote the marginal prior variance of $\boldsymbol{\mu}_h$ by $\mathbf{K}_h = K(B_h, B_h)$, the prior covariance of $\boldsymbol{\mu}_h$ and $\boldsymbol{\mu}_s$ by $\mathbf{K}_{h,s} = K(B_h, B_s)$, etc. The obvious difficulty working with (6) directly is that the covariance matrix is large and dense and we need to be able to compute its inverse in order to evaluate the prior. We would like to make inferential statements about $\boldsymbol{\mu}_h$, but the dimension of the submatrix \mathbf{K}_h ($n_h \approx 200,000$) alone is prohibitive on most hardware architectures—such a matrix would require over $(1.8 \times 10^5)^2 \times 32 = 129.6$ Gb of memory just to store in a single precision floating point format. Though the memory requirement could be reduced by storing just the upper or lower triangle, to sample $\boldsymbol{\mu}_h$ Cholesky decomposition of \mathbf{K}_h would still require $\approx 1.9 \times 10^{15}$ floating point operations (FLOPs) to compute.

In (6), the covariance matrix has rank of at most n_h , and the implied conditional density $\pi(\boldsymbol{\mu}_s | \boldsymbol{\mu}_h)$ is degenerate on $\mathbf{K}_{s,h}\mathbf{K}_h^{-1}\boldsymbol{\mu}_h$. Additionally, we represent the product $\mathbf{K}_h^{-1}\mathbf{K}_{h,s}$ by matrix $\mathbf{W}^\top = [w(\mathbf{v}_s)]_{\mathbf{v}_s \in B_s}$. To induce sparsity and save computational resources, we defined \mathbf{W} in terms of neighborhoods of voxels in B_h . For any $\mathbf{v} \in \mathcal{B}$, let $N_h(\mathbf{v})$ denote a set of locations in B_h in an r -neighborhood of location \mathbf{v} , $N_h(\mathbf{v}) = \{\mathbf{v}_h \in B_h : \|\mathbf{v}_h - \mathbf{v}\|_2 \leq r\}$. If $N_h(\mathbf{v})$ is empty, then we defined $w(\mathbf{v}) = \mathbf{0}$; otherwise let $\mathbf{K}_{N_h(\mathbf{v})} = [k(\mathbf{v}_i, \mathbf{v}_j)]_{\mathbf{v}_i, \mathbf{v}_j \in N_h(\mathbf{v})}$, let $\mathbf{k}_{N_h(\mathbf{v})} = [k(\mathbf{v}_i, \mathbf{v})]_{\mathbf{v}_i \in N_h(\mathbf{v})}$, and let $\tilde{\mathbf{w}} = \mathbf{K}_{N_h(\mathbf{v})}^{-1}\mathbf{k}_{N_h(\mathbf{v})}$ denote a vector with implicit dependence on $N_h(\mathbf{v})$ where each element corresponds with one location in $N_h(\mathbf{v})$. For non-empty $N_h(\mathbf{v})$, each element of $w(\mathbf{v})$ similarly corresponds with one location in B_h . We defined those elements to be,

$$w_i(\mathbf{v}) = \begin{cases} \tilde{w}_j & \text{if the } j^{\text{th}} \text{ location in } N_h(\mathbf{v}) \text{ corresponds to the } i^{\text{th}} \text{ location in } B_h \\ 0 & \text{otherwise.} \end{cases} \quad (7)$$

With $\mathbf{W}^\top = [w(\mathbf{v}_s)]_{\mathbf{v}_s \in B_s}$, the product $\mathbf{W}\boldsymbol{\mu}_h$ can be interpreted as a local kriging approximation of $\boldsymbol{\mu}_s$ conditional on $\boldsymbol{\mu}_h$. Our definition of \mathbf{W} is conceptually somewhat inspired by work on Nearest Neighbor Gaussian Processes by [Datta et al. \(2016\)](#); [Finley et al. \(2019\)](#). A sensitivity analysis over choice of r is available in the Supplementary Material ([Whiteman et al., 2022](#)).

The matrix \mathbf{W} can be entirely precomputed given the kernel parameters, ψ, ν , and a neighborhood radius, r . Equipped with the matrix \mathbf{W} , samples from (6) can be drawn by first sampling $\boldsymbol{\mu}_h \sim \mathcal{N}(\mathbf{0}, \mathbf{K}_h)$, and then computing $\boldsymbol{\mu}_s = \mathbf{W}\boldsymbol{\mu}_h$. In practice we treat r as a hyperparameter and condition analyses on it. In our data example (see section 4) we took the radius r to be roughly one FWHM length based on estimated prior covariance and hyperparameters $\boldsymbol{\theta}$ (section 4.1). This choice was motivated by the desire to keep r roughly in line with the width of (5) while keeping \mathbf{W} only modestly expensive to compute: for this choice of r , typical neighborhood sizes $|N_h(\mathbf{v})|$ were on the order of 300–700 voxels in patient data. We next outline an efficient posterior computation algorithm for $\boldsymbol{\mu}_h$.

2.3. Posterior computation

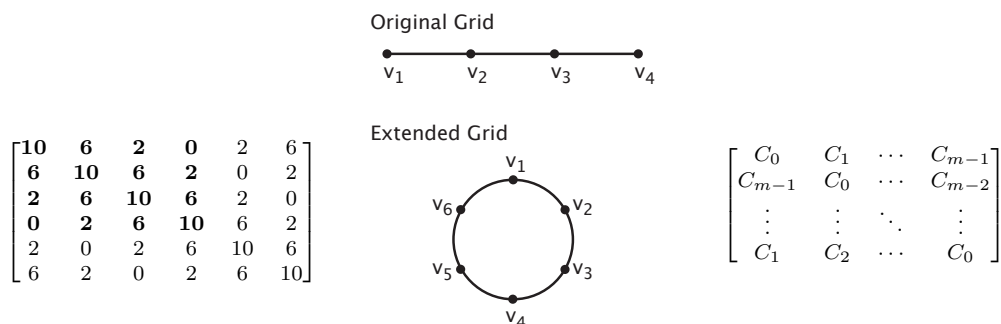


Fig 2: Example circulant matrix embedding. The left-most panel shows an example 4×4 Toeplitz matrix (bold) embedded within a 6×6 circulant matrix. In this simple example, the inner Toeplitz matrix might correspond with locations on a 1D grid (center panel). Conceptually, the outer circulant matrix can be taken to correspond with an extended grid, where an extended set of vertices have been “wrapped around” a circle. In the more general case (right-most panel), blocks C_i of a circulant-family matrix have symmetry such that $C_{m-i} \equiv C_i$.

To facilitate computation we embedded the random field $\boldsymbol{\mu}_h$ within a much larger random field, which we will call \mathbf{u} . Our goal in doing so was to be able to replace expensive matrix operations with computations involving discrete Fourier transformations (DFTs) as we show below. Conceptually, the augmented parameter space we chose can be viewed to correspond with an extended grid of locations with toroidal geometry. In our data application, the resulting extended grid has about 8.4×10^6 elements (grid dimensions $256 \times 256 \times 128$). We treat this extended grid as if it were a part of B_h in the prior, with the result that the covariance of the field \mathbf{u} has a nested block-circulant structure. In the discussion to follow, we will use \mathbf{C} to denote the prior variance of \mathbf{u} . With this construction, we have added a large number of auxiliary parameters, but have not changed the effective prior on $\boldsymbol{\mu}_h$: the matrix \mathbf{K}_h is a principal submatrix of \mathbf{C} . Any Toeplitz-family matrix can be embedded in a larger circulant-family matrix in this way. For additional exposition, Fig. 2 shows a simple example of this type of circulant embedding. In the figure, the left and center panels illustrate circulant embedding for a 1D grid. If working on a 2D grid, then schematically each block C_i in the right-most panel of Fig. 2 will be a circulant matrix; on a 3D grid each block will itself be block-circulant, etc. This construction can be used to enable efficient simulation of

random Gaussian fields over dense grids as others have shown (e.g. [Wood and Chan, 1994](#); [Rue and Held, 2005](#)) and as we summarize below.

Circulant matrix–vector products can be computed efficiently with DFT software. Given the first row or column \mathbf{a} —the so called base—of a circulant matrix \mathbf{A} the product $\mathbf{A}\mathbf{x}$ can be expressed as the discrete convolution $\mathbf{a} * \mathbf{x}$. Equivalently, by the discrete convolution theorem, $\text{DFT}(\mathbf{A}\mathbf{x}) = \text{DFT}(\mathbf{a}) \odot \text{DFT}(\mathbf{x})$, where \odot denotes an elementwise or Hadamard product. The principle is the same with a nested block-circulant matrix like \mathbf{C} : the matrix has a base, \mathbf{c} , that is efficient to work with using 3D DFTs. In the present case, \mathbf{c} can be precomputed (see the Supplementary Material) from the original grid dimensions and covariance function $K(\cdot, \cdot)$. As with any circulant matrix, \mathbf{C} can be diagonalized by two Fourier matrices. If \mathbf{F} denotes a scaled 3D DFT matrix, and \mathbf{F}^H its adjugate, $\mathbf{F}^H \mathbf{C} \mathbf{F} = \text{diag}(\boldsymbol{\lambda})$, where $\boldsymbol{\lambda}$ are the (complex) eigenvalues of \mathbf{C} . With only the base \mathbf{c} in memory, $\boldsymbol{\lambda} = \mathcal{F}(\mathbf{c})/N$ can be computed directly, where N is the number of elements in \mathbf{c} , and $\mathcal{F}(\cdot)$ denotes the 3D discrete Fourier transform. We provide a simple algorithm to construct \mathbf{c} for any dense 3D grid in the Supplementary Material ([Whiteman et al., 2022](#)).

[Wood and Chan \(1994\)](#) took advantage of this relationship to propose an efficient algorithm for simulation of random Gaussian fields when the covariance of the field can be embedded within a circulant matrix. For example, in our setting, we could sample from the prior $\pi(\boldsymbol{\mu}_h \mid \boldsymbol{\theta})$ by first drawing $\mathbf{z} \sim \mathcal{CN}(\mathbf{0}, \mathbf{I})$, where $\mathcal{CN}(0, v)$ denotes the circularly symmetric complex normal distribution with variance $2v$. Let $\mathcal{F}^{-1}(\cdot)$ denote the 3D inverse DFT, let $\mathbf{a}^{\odot b} = [a_i^b]$ denote elementwise or Hadamard exponentiation, and let $\mathcal{R}e(\mathbf{a})$ extract the real part of a complex vector \mathbf{a} . With $\boldsymbol{\lambda}$ computed as above, we could then set $\mathbf{u} \leftarrow \mathcal{R}e[\mathcal{F}\{\boldsymbol{\lambda}^{\odot 1/2} \odot \mathcal{F}^{-1}(\mathbf{z})\}]$, and obtain a prior sample of $\boldsymbol{\mu}_h$ by simply discarding extraneous elements of \mathbf{u} .

There is no direct extension of the above [Wood and Chan \(1994\)](#) algorithm for posterior simulation in our setting. In part, this is because we use different noise variance terms for our two data sources (2). Unless the diagonal noise terms are exactly equal, the joint posterior variance of $(\boldsymbol{\mu}_h^T, \boldsymbol{\mu}_s^T)^T$ will not be Toeplitz in general. We still draw inspiration from the work of [Wood and Chan \(1994\)](#), however, and use the circulant matrix relationships above to write an efficient Hamiltonian Monte Carlo algorithm for posterior inference. Details of this algorithm are presented in the Supplementary Material ([Whiteman et al., 2022](#)), but the key components are: (i) as discussed, we embed $\boldsymbol{\mu}_h$ in a higher dimensional random Gaussian field with a circulant covariance matrix; and (ii) we construct a circulant “mass matrix” for our HMC. Modification (i) allows us to be able to evaluate the log prior and compute its gradient, and modification (ii) dramatically improves mixing of the HMC chains. As a result, our algorithm reduces the computational requirement to evaluate the log prior on $\boldsymbol{\mu}_h$ roughly to < 0.01 Gb and $\approx 2 \times 10^9$ FLOPs. We now turn to remark on how we summarize inference from our model in practice.

2.4. Functional region detection

fMRI detects functionally relevant brain regions by recording changes in oxygenated blood flow (BOLD signal). In a typical study, practitioners identify these regions by thresholding voxelwise statistical summaries in a manner that controls the false discovery rate (e.g. [Genovese, Lazar and Nichols, 2002](#)). For presurgical applications, it is at least as important to limit false negative reports, since errors of this kind may potentially lead to damage of healthy tissue. To this end, we adapted a decision theoretic approach following previous work ([Müller, Parmigiani and Rice, 2006](#); [Liu et al., 2016, 2019](#)). We consider the loss function,

$$L(\mathbf{m}, \boldsymbol{\delta}) = \sum_i -f(m_i)\delta_i - \{1 - f(m_i)\}(1 - \delta_i) + k_1 f(m_i)(1 - \delta_i) + k_2 \{1 - f(m_i)\}\delta_i + t\delta_i, \quad (8)$$

where (k_1, k_2, t) are tunable constants, the $m_i = |\mu_{h,i}|/\sqrt{\text{var}(\mu_{h,i})}$ are posterior t -statistic analogs measuring pointwise signal strength in μ_h , and the $\delta_i \in \{0, 1\}$ are pointwise statistical decisions (i.e. $\delta_i = 1$ reports a finding at voxel i , and $\delta_i = 0$ otherwise). The function $f(\cdot)$ can be any monotonically increasing function restricted to $[0, 1]$, and is intended to act as a proxy for $\pi(\delta_i = 1 | \mathbf{Y}_h, \mathbf{Y}_s, \boldsymbol{\theta}, r)$. Again, following previous work (Liu et al., 2016, 2019), we take $f(m) = m/M$, where $M = \max_i\{m_i\}$.

The loss function (8) is composed of five terms, each with a distinct importance: $-\sum_i f(m_i)\delta_i$ and $-\sum_i\{1 - f(m_i)\}(1 - \delta_i)$ induce gains for correct discoveries and correct non discoveries, respectively; $k_1 \sum_i f(m_i)(1 - \delta_i)$ penalizes false negative errors; $k_2 \sum_i\{1 - f(m_i)\}\delta_i$ penalizes false positive errors; and $t \sum_i \delta_i$ penalizes the total number of discoveries. Optimal decisions δ_i^* minimize the posterior risk and follow,

$$\delta_i^* = \mathbb{1}\{\bar{f}_i \geq (1 + k_2 + t)/(2 + k_1 + k_2)\}, \quad (9)$$

where \bar{f}_i is the posterior expectation $\mathbb{E}\{f(m_i) | \mathbf{Y}_h, \mathbf{Y}_s, \boldsymbol{\theta}, r\}$, and the parameters (k_1, k_2, t) suggest a threshold based on a trade off between false negative and false positive errors.

Thresholds can be tuned with domain expert guidance and/or varied dynamically, as a single static threshold may not be sufficient for a surgeon’s needs (e.g. Stippich, 2015). As a practical note, setting $k_2 = t = 1$ and varying k_1 over the range $[5, 12]$ can provide good guidance, with $k_1 = 7$ a reasonable default. In one of our patient data analyses (below), we set $t = 1$, $k_1 = 12$, and $k_2 = 1$ for inference. As per our coauthor and collaborating neuroradiologist’s advice, this tuning parameter choice penalizes false negative errors 12 times more heavily than false positive errors. The other patient in our data was somewhat younger and less ill, with no interictal speech or language impairments. Consequentially her z -statistic images appeared to have a better signal to noise ratio. For this patient, the suggestion was to set $k_1 = 7$ and use a seven fold penalty ratio (not shown). In both cases, the corresponding activation thresholds were confirmed visually by comparison with results from intraoperative electrocortical interference mapping.

3. Simulation studies

We quantified the advantages of our proposed method with easier to visualize simulations in two dimensions. Our goal in simulation was to evaluate how well the proposed model and alternative methods recovered activation patterns in data. Typical fMRI studies use significance testing as a means to identify functionally relevant brain regions. To mimic this setting, our simulation designs considered active regions embedded within low variance signal (see Fig. 3). As we discuss below, we further tried to mimic the patient data by roughly matching simulated spatial signal smoothness and signal-to-noise ratios to the real data.

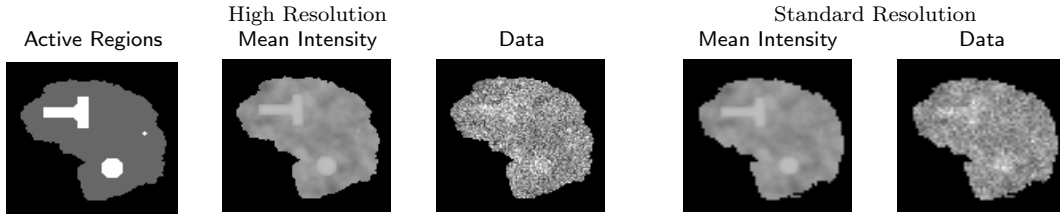


Fig 3: Simulation design example with $\text{SNR}_h = 0.1$ and $\text{SNR}_s = 0.2$. Non-activation smooth signal has marginal variance 0.2 and 6 mm FWHM Exponential correlation; activation signal has mean 2.

3.1. Simulations on 2D grids

Figure 3 illustrates our general approach to data simulation. In the figure, active regions were drawn in a midsagittal plane including a T-shaped region, a circular region, and a four voxel square. These signals were created by smoothing binary images with a six millimeter full width at half maximum (FWHM) Gaussian kernel, scaling by a factor of two, and thresholding the result at 0.4. We then embedded the active regions within random draws from a 2D random field with mean zero, marginal variance 0.2, and 6 mm FWHM Exponential or Gaussian correlation functions. We treated the resultant images as true nonzero mean intensity images, with “active” voxels given only by the smoothed T, circle, and square shapes; on average about 11% of activation-adjacent voxels would have had signal strength within ± 0.25 standard deviations of their active neighbors. As per the patient data, we treated voxels in this plane as (1.8×1.8) mm for high resolution (4,722 voxels total), and as (3×3) mm for standard resolution (1,853 voxels). With our design, there were exactly 450 active voxels in the high resolution slice (9.5%; see Fig. 3).

We adopted this method to generate “high resolution” mean images, or μ_h as in section 2.3, and projected μ_h into “standard resolution” space by multiplying by \mathbf{W} as in section 2.2 to generate corresponding standard resolution mean images. In all simulation settings, \mathbf{W} was constructed using the true 6 mm FWHM Exponential or Gaussian background signal correlation functions, and an extent radius r defined as the distance after which the correlation would drop below 0.05. To simulate observed outcome data, we added independent Gaussian noise to the mean intensity images, modulated the noise variances to control SNRs of the simulated high and standard resolution images, and ran 100 replicates per parameter combination. We took the SNR to be the ratio of the second moment of the mean to the variance of the noise, and set this to be one of $\{0.1, 0.2\}$ for high resolution images (SNR_h). We parameterized standard resolution noise in terms of the ratio of standard to high resolution SNR ($\text{SNR}_s:\text{SNR}_h$), and set this ratio to one of $\{1, 2, 4\}$. In the first case, the standard resolution image would not provide additional signal-to-noise support as it typically would in real data. We considered this a worst case scenario. The latter two settings were chosen so that the standard resolution image provided increasingly large signal-to-noise support, where we expected our dual resolution method to dominate. In our analysis of the patient 1 data, based on the fits of our high and standard single resolution alternative models, we estimated $\text{SNR}_h \approx 0.18$ and $\text{SNR}_s \approx 0.44$ based on their posterior means (ratio $\text{SNR}_s:\text{SNR}_h \approx 2.4$).

3.2. Recovery of simulated activation regions in 2D images

<i>Model</i>	<i>Kernel</i>	<i>SNR_s:SNR_h</i>	<i>SNR_h</i>	<i>MSE</i>	<i>False –</i>
Dual	Exponential	1	0.1	0.20	31.8% (0.4)
High	Exponential	1	0.1	0.23	34.0% (0.5)
Naive	Exponential	1	0.1	0.30	43.6% (0.4)
Std	Exponential	1	0.1	0.47	43.1% (0.6)
Dual	Exponential	2	0.1	0.18	30.6% (0.4)
High	Exponential	2	0.1	0.23	34.0% (0.5)
Naive	Exponential	2	0.1	0.29	42.7% (0.4)
Std	Exponential	2	0.1	0.43	40.6% (0.4)

TABLE 1

Selected results for estimation and inference quality in 2D simulations. Results for the High resolution method do not change across the different SNR ratios, but are repeated to facilitate comparison. Model denotes the image combination used in the analysis, and Kernel gives the correlation pattern of low variance background signal. MSE refers to mean squared error computed over the entire high resolution mean parameter vector; the simulation standard error of this metric was on the order of 10^{-3} for all simulation settings and so was omitted for brevity. False – reports the mean (SE) false negative error rate when the number of discoveries was fixed at 450. One hundred replicates per parameter combination; additional results with different kernel and SNR_h parameter settings are summarized in the Supplementary Material.

In each simulation, models were conditioned on the true $\theta = (\tau^2, \psi, \nu)^\top$ used to generate the low variance mean fields. We chose to condition on the true θ so as to explicitly focus our simulation results on estimation of and inference on the image mean intensities. We compared performance of our dual resolution model (1) against single resolution alternative methods: (i) a related Gaussian process model that only considered the high resolution data, (ii) the same model but considering only standard resolution data (kriging the posterior mean of μ_s to the locations in B_h), and (iii) a method that we term naive data averaging. For the alternative high and standard resolution models, we used a Gaussian process to model the the mean of the data as in (3). For the naive alternative, we estimated the matrix \mathbf{W} (defined in section 2.2) from the data and used it to interpolate standard resolution data into the high resolution space. We then treated a simple pointwise average of the high and interpolated standard resolution images—i.e. $\bar{\mathbf{Y}}_{hs} = (\mathbf{Y}_h + \mathbf{W}^\top \mathbf{Y}_s)/2$ —as data in the alternative high resolution model (i). This approach is conceptually similar to previous work in this area (Liu et al., 2019). The high resolution method (i) served as our primary comparison point both because of its inherent spatial resolution and because it tended to be the best competing method in our simulations (see section 3).

Table 1 presents selected results for estimation and inference quality in our 2D simulation settings. Results are presented predominantly for the setting with $\text{SNR}_h = 0.1$, the $\text{SNR}_s:\text{SNR}_h$ ratio set to two, and an Exponential correlation function to roughly approximate our patient data (also reflected in Fig. 3). We provide a comparison point with the SNR ratio equal to one for additional interest. More extensive results are available in the Supplementary Material (Whiteman et al., 2022). In the table, MSE denotes the mean squared error of the estimated μ_h , computed over pixels in our simulated high resolution slices. We treat MSE as a measure of estimation quality, and report that in all simulation settings considered, MSE was lowest for the dual resolution models. This result indicates that when the same mean intensity function underlies both high and standard resolution images and the kernel function is estimated accurately, the model that used joint information from both imaging modalities outperformed possible single resolution alternatives. Interestingly, when the background intensity was generated with an Exponential kernel, as in Table 1, the model that used only high resolution data was the second best performer, underscoring the importance of spatial precision in estimation.

We also report false negative rates—the measure of inference we are most concerned with in our framework—for each model in Table 1. In the table, we set parameters k_1 , k_2 , and t in our decision rule (9) independently for each model type so as to control the total number of discoveries to exactly 450 (the same as the number of pixels we considered truly active in the simulations). The actual decisions corresponding to these thresholds are shown in Fig. 4 (right) for a single representative simulation iteration. We emphasize that thresholds here were chosen as an objective point of comparison across the alternative methods, not by optimizing any kind of inferential criteria. In Fig. 4 (left), we show that the dual resolution model would give superior inference for any set of decision rule thresholds that fix the false negative rate at a single value across all methods.

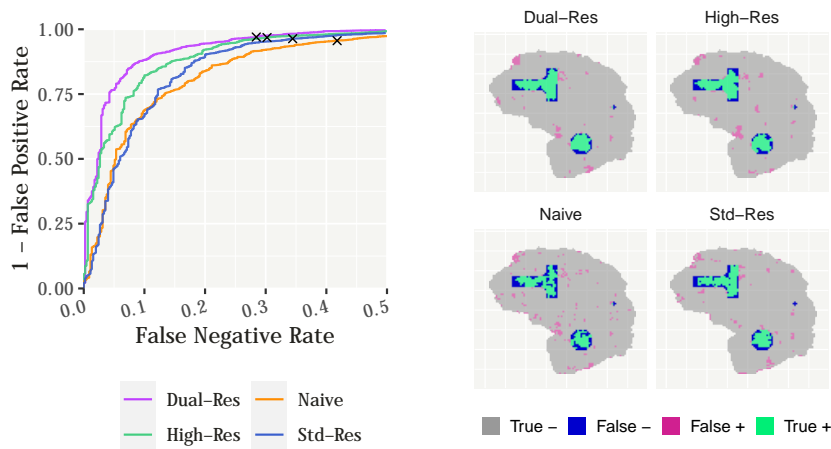


Fig 4: Inference quality in 2D simulations. (*Left*) Receiver operating characteristic (ROC) curves comparing dual and single resolution methods to a naive data averaging approach in a setting that matches the data in Fig. 3. The curves show that for almost any given false negative rate, the dual resolution method can have a uniformly lower false positive rate than alternative single resolution methods. The \times 's mark the thresholds used to generate the inferential summary on the (*right*). These thresholds limit the total number of discoveries to 450 across all four methods.

4. Patient data analysis

As noted, our first motivating dataset—“patient 1”—comes from a right handed 62 year old woman who presented primarily with difficulties reading (pure alexia). This patient was found to have a large tumor in her left middle and inferior temporal gyrus; following partial surgical resection, the tumor was classified as a glioblastoma multiforme. Our second motivating dataset—“patient 2”—comes from an 18 year old right handed woman who presented after a general seizure. This patient was found to have a relatively large cavernoma adjacent to insular cortex and the transverse temporal gyrus. Both patients were scanned prior to surgery while performing a reading task with a 30 second on/off block design to map brain areas associated with reading and subsequent language processing. The task consisted of silent reading in interleaved blocks of non-final embedded clause sentences (on; eight blocks) and strings of consonants (control; eight blocks).

Details of our fMRI acquisition protocol and preprocessing are given in Appendix A. Preprocessing resulted in one unsmoothed z -statistic image for each fMRI resolution that summarized task-related activation over the course of the functional scans. We fit our model to the patient 1 z -statistic image data to compare relative performance against a set of similar single-resolution alternative methods. With this analysis, our goal was to show how our method can be applied to identify peritumoral activations in patient data and to illustrate potential benefits to inference using combined spatial resolutions. In addition, we fit our model to the z -statistic images from patient 2 to illustrate the method’s capacity to recover an estimate of activation in regions with signal loss. Signal loss in fMRI data can occur where tissue types with different magnetic field susceptibilities neighbor one another. This is a common problem encountered in presurgical applications, and can potentially lead to exclusion of areas of interest from the analysis (e.g. Haller and Bartsch, 2009; Stippich, 2015).

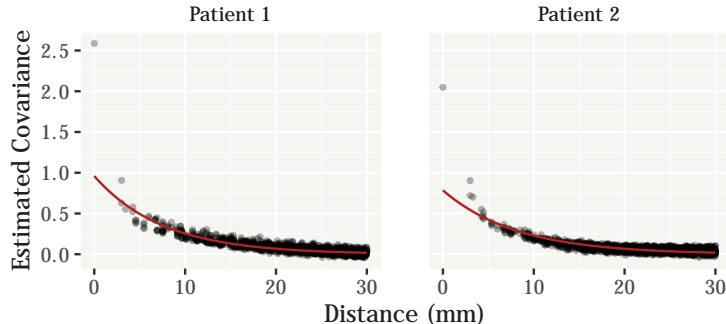


Fig 5: Covariograms show empirical covariances between neighboring standard resolution voxels as a function of distance overlaid with a parametric estimate of the covariance function.

4.1. Covariance estimation

We chose to estimate the Gaussian process covariance hyperparameters θ in the spirit of empirical Bayes using the method of minimum contrast. Minimum contrast estimation (MCE) originates from Diggle (1981) as a moment estimation approach to spatial modeling. The method seeks to estimate parameters of a function with a known form by minimizing some discrepancy criterion given data. In our case we extracted empirical covariances between voxels at different distances (“empirical covariogram”). We then selected θ to minimize a nonlinear least squares objective over (5), treating the empirical covariogram as pseudo data. Our Supplementary Material (Whiteman et al., 2022) gives a detailed overview of this procedure for interested readers, as well as a brief sensitivity analysis over our choice of covariance function in (5).

This method is not without difficulty. For example, asymptotic theory suggests that empirical covariogram estimation is biased (e.g. Cressie and Glonek, 1984). Although this bias does not decrease with increased sampling density (“infill asymptotics”), it can be decreased by sampling data over increasing domains (Mardia and Marshall, 1984; Stein, 1999; Zhang, 2004). This point is worth acknowledging because the kriging identity encoded in our prior (6) makes estimation of the correlation relatively important. On the other hand, MCE is computationally efficient and scalable to large datasets, and we found that it produced reasonable estimates of the true covariance function in simulation (see the Supplementary Material). One reason for this may be that with fMRI data we have a tremendous amount of spatial information collected on a dense grid. Although we can only estimate empirical covariances at a fixed set of distances, we typically have tens of thousands of unique pairs of voxels separated by those distances. In Fig. 5, we used the standard resolution images to estimate θ as we expect these data to have better SNR and there is no theoretical benefit to adding infill locations as with the high resolution images. In doing so, we make an appeal to the notion of a parent process (Banerjee et al., 2008) for $\pi\{\mu(\cdot)\}$, which could be defined such that in the prior $\text{cov}\{\mu(\mathbf{v}), \mu(\mathbf{v}')\} = k(\mathbf{v}, \mathbf{v}')$ for all $\mathbf{v}, \mathbf{v}' \in \mathcal{B}$.

For patient 1, an initial unrestricted estimate of θ yielded an estimated kernel exponent of $\nu \approx 1.25$; for improved interpretability we reran our MCE procedure fixing $\nu = 1$ to yield $\theta = (0.887, 0.135, 1)^T$. Optimization was performed using the COBYLA algorithm (Powell, 1994) as implemented by Johnson in the popular NLOpt library. The resulting covariance function is shown in the left panel of Fig. 5, and corresponds to a 10.47 mm full width at half maximum (FWHM) exponential correlation function. This estimate of θ was used for all of our analyses of patient 1’s data; correspondingly, we set the neighborhood radius r to 10.35 mm in analyses of this patient’s data.

Similarly, we estimated $\theta = (0.785, 0.132, 1)^T$ for patient 2. The resulting covariance function

(also shown in Fig. 5, right) corresponds to a 11.28 mm FWHM exponential correlation function; we set r to 11 mm for analysis of this patient’s data. In Fig. 5, the exponential kernels appear to fit the empirical covariograms quite well. The points at distances of 0 mm are not outliers but estimates of the “sill” or marginal variance of the \mathbf{Y}_s which in our model is $\tau^2 + \sigma_s^2$. Consequentially, our algorithm constrains τ^2 to be strictly less than the empirical variance of \mathbf{Y}_s , or whichever image is used to construct the covariogram. In addition, the exponential models in Fig. 5 tend to mildly but systematically underestimate the empirical covariances at displacements around 3 mm. We discuss how these data points can be modeled more accurately, and elaborate on why it may or may not be optimal to do so in the Supplementary Material (Whiteman et al., 2022).

4.2. Patient 1: Inference on the functional signals

We fit our model to the data from patient 1 described in section 2 with custom software written in C++ that uses the Eigen (Guennebaud et al., 2010) and FFTW (Frigo and Johnson, 2005) libraries for linear algebra and DFT operations, respectively. For these analysis, we set the number of leapfrog steps $L = 25$ and ran three independent HMC chains of 4,000 iterations each, discarding the first 1,000 as burnin, and thinning the output to every third iteration thereafter. Univariate Gelman–Rubin statistics (Gelman et al., 1992) were used to evaluate voxelwise convergence of μ_h . This statistic was ≤ 1.03 for every voxel, suggesting approximate convergence. Additionally, trace plots of means from six randomly selected voxels are shown in in the Supplementary Material (Whiteman et al., 2022) and show good mixing of the Markov chains.

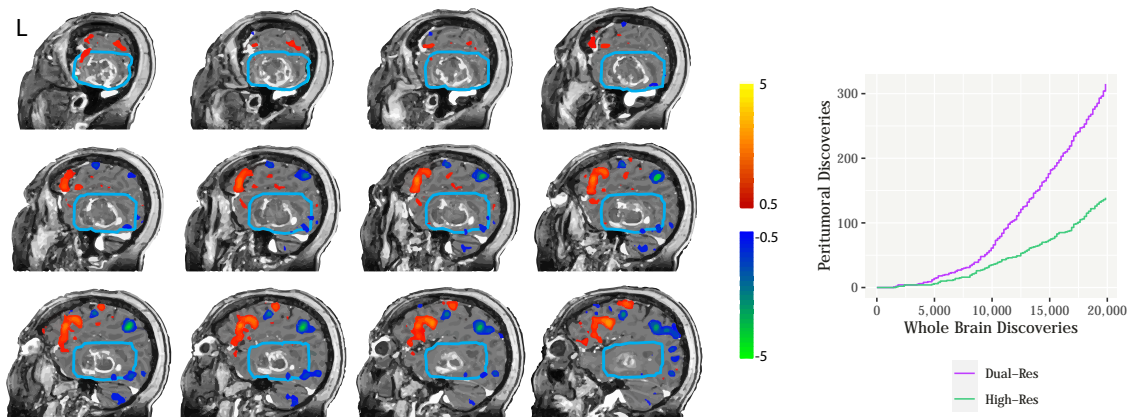


Fig 6: Patient 1: (*Left*) Thresholded posterior mean image shows peritumoral activation identified using our dual resolution method. The tumor is the region of mixed hypo- and hyperintensity in the temporal lobe across slices; the peritumoral region is outlined in each panel (in cyan). Functional activations are shown in warm colors, and functional deactivations are shown in cool colors, with units on the z -statistic scale. Activation regions are shown setting k_1 in our decision rule (9) to 17 to enhance the visualization. Slices are shown proceeding lateral-to-medial through the left hemisphere in left-to-right, top-to-bottom order. (*Right*) Cumulative counts of discoveries at varying decision thresholds. Voxelwise discoveries in the peritumoral region plotted against whole brain discoveries for both dual and high resolution methods.

Fig. 6 (*left*) shows posterior mean activation maps for a series of sagittal slices through the patient’s tumor in left temporal lobe. Activations are overlaid on a high resolution, gadolinium enhanced T1-weighted anatomical scan. In the figure, we have circled a peritumoral region that was deemed to determine the surgical access considered. The patient’s tumor can be seen within

this circled region in all slices. As in our simulation studies, we compared performance of our dual resolution model against single resolution alternatives: models considering only the high or standard resolution data, and an additional setting using a naive average as data.

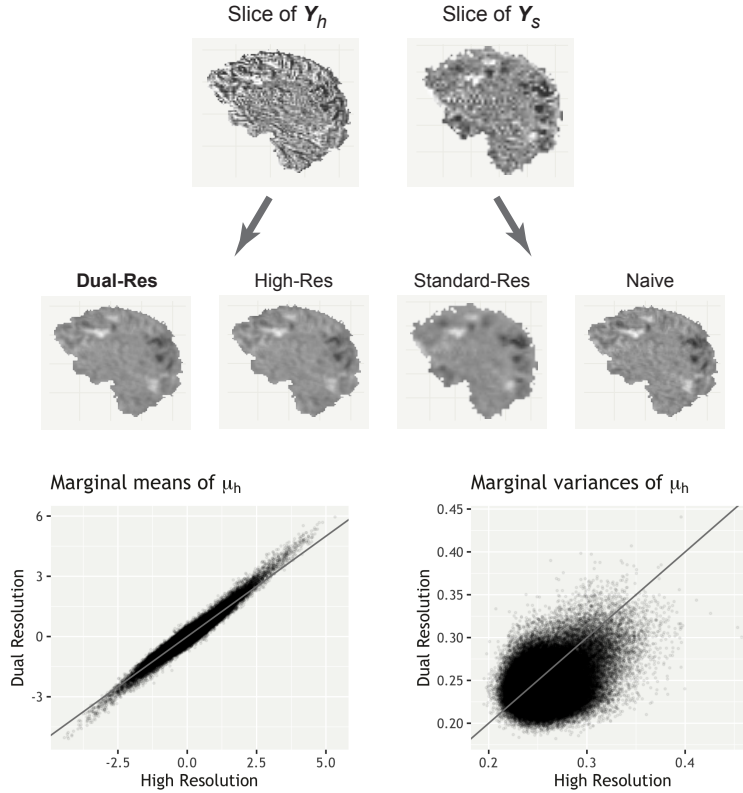


Fig 7: Patient 1: visual comparison of posterior means in a single sagittal slice from four models fit to different combinations of whole brain patient data (*middle*). The (*top*) row of the figure shows the raw data from the same slice at both high and standard resolution. Grayscale intensity is shared across all subfigures. The (*bottom*) row shows a comparison of voxelwise posterior means (*bottom, left*) and variances (*bottom, right*) of the elements of μ_h estimated using the proposed model and a single (high) resolution alternative. The gray lines show identity relationships for comparison; variances were lower using the dual resolution model in about 72.4% of voxels.

In Fig. 6 (*right*), we show that no matter the threshold applied to whole brain posterior activation maps, our dual resolution method identified at least as many active voxels in the peritumoral region than if we had ignored the standard resolution data. A visual comparison of the posterior mean of $\mu(\cdot)$ for all four methods is shown in Fig. 7. We chose a single sagittal slice to represent this comparison although the analysis was over the whole brain. Qualitatively, posterior means from the dual and high resolution analyses appear substantially sharper than for the standard resolution analysis. At the same time, differences are apparent in the dual and high resolution posterior means, particularly around the edges of areas with high magnitude signal. We also plot voxelwise comparisons of dual and high resolution posterior means and variances of μ_h in Fig. 7. In the figure, voxels with high signal strength typically had higher magnitude posterior means estimated with the dual resolution model; marginal variances of the $\mu_{h,i}$, moreover, were lower with the dual resolution model in about 72.4% of voxels. With respect to mean image smoothness, we estimated (using our MCE procedure; see section 4.1) the standard resolution posterior mean image had a kernel FWHM

of about 17.3 mm, and the high resolution posterior mean image had a kernel FWHM of about 13 mm. Appropriately, the dual resolution posterior mean image had a kernel FWHM between these two, at about 14.4 mm. Relating back to Fig. 1, our initial goal in modeling joint data sources was to reduce noise inherent in the high resolution signal and leverage signal strength from the standard resolution data. Taken all together, these results demonstrate that we have met that goal.

Additional patient 1 model fit and diagnostic evaluations are given in the Supplementary Material (Whiteman et al., 2022). In particular, we evaluated the residual independence approximation present in our model likelihood by running our kernel estimation procedure (see section 4.1) on the model residual images. These analyses suggested that residual correlation decayed to near zero within the smallest voxel dimension widths, leading us to conclude that residual independence was a reasonable approximation in our data. Full results are available in the Supplementary Material (Whiteman et al., 2022).

4.3. Patient 2: Recovery of lost signal

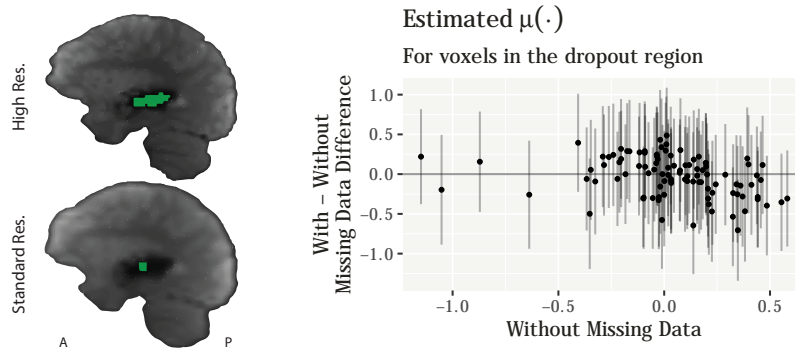


Fig 8: Patient 2: (*Left*) Core regions of fMRI signal loss across the left temporal and insular cortex are highlighted on high and standard resolution T2*-weighted slices. (*Right*) Comparison of the mean parameter for voxels in the core high resolution dropout region. We fit our dual resolution model to parallel versions of the data with and without missingness. The posterior mean estimate of $\mu(\cdot)$ without missing data is shown on x -axis, with the difference in the estimates shown on y -axis. Error bars give \pm one standard error of the difference estimated across five HMC chains.

Similar to our analysis of patient 1, we fit our dual and single resolution models to the data from patient 2. In this case, we ran five independent HMC chains for each model and set the chain length, burnin, thinning rate, and number of leapfrog steps identically as above. Univariate Gelman–Rubin statistics were ≤ 1.05 , again suggesting approximate voxelwise convergence of μ_h . Our primary goal with this analysis was to illustrate our method’s ability to recover estimates of activation from regions of signal loss.

In this particular data set, the patient’s cavernoma caused a region of GE-EPI signal dropout, with blooming along the left insular and upper temporal lobe (see Fig. 8, *left*). This is a common occurrence in clinical fMRI: brain lesions can induce signal loss and magnetic susceptibility artifacts in gradient echo imaging. The functional signal is not “missing,” per se, but local signal hypointensities can cause image preprocessing software to exclude affected areas from analysis (Haller and Bartsch, 2009). Such was the case here, and we leveraged this data structure to highlight our model’s predictive ability. By adjusting brain/background thresholding in FSL, we created two versions of this patient’s task contrast data: one where data in the core dropout region was completely masked out of all analyses (with missing data), and one where voxels in this same region were included in

all analyses (without missing data). In this case, we were able to create parallel versions of the data for this patient, though in more general practice it may sometimes be difficult to engineer the data without missingness (Haller and Bartsch, 2009).

We fit our models to both versions of the data to compare resulting functional estimates. In the case of missing data, the Gaussian process formulation of our model enables natural prediction of values of $\mu(\cdot)$ for voxels with missing data. In the high resolution image, the region masked out due to signal loss encompassed exactly 100 voxels, had a maximum length (measured anterior to posterior) of around 25–26 mm, and was on average about 9.4 mm wide (lateral to medial) and 4.5 mm tall (dorsal to ventral). In the low resolution image, masked dropout was limited to only two voxels given default brain/background thresholding in FSL. With typical preprocessing pipelines we would generally expect more signal loss voxels to be excluded from high resolution images. In Fig. 8 (*right*) we show, for our dual resolution method, the correspondence of predicted/estimated voxelwise means in the dropout region for the two data variants. The figure shows excellent correspondence: the Pearson correlation between the predictions and the estimates is 0.673, suggesting our method has a strong capacity for signal recovery in dropout regions of this size. Similar predictions/estimations using only the high resolution data also show good correspondence, but were made with higher variance relative to our dual resolution approach in 81 of the 100 dropout region voxels.

Similarly, across the whole brain, the marginal variances of μ_h for patient 2 were lower with our dual resolution approach in about 62.4% of voxels (compared to the high resolution model). Moreover, we estimated that the dual resolution posterior mean image smoothness had a kernel FWHM of about 7.5 mm, while the high and standard resolution posterior mean image smoothness FWHMs were about 7.6 mm and 13.5 mm, respectively. Overall, estimation and inference about μ_h was more similar between our dual and high resolution models here than for the previous patient. Altogether, results from our analysis of the patient 2 data again suggested our inference benefited from combining information from both spatial resolutions, though the benefit may be less pronounced compared to in patient 1. Based on our single data source high and standard resolution alternative methods, we estimated that for patient 2, the standard resolution data provided only a modest 5.4% improvement in SNR compared to the high resolution data. By contrast, for patient 1, the standard resolution data provided approximately a 139% improvement in SNR, lending context to the above result.

5. Discussion

Preoperative fMRI presents many interesting and unique statistical challenges from an applied perspective. Presurgical planning requires spatially precise localization of patient specific functional neuroanatomy, but the current physical limitations of MR imaging technology lead to reductions in the signal to noise ratio (SNR) with increases in spatial resolution. This inherent limitation has led to the hypothesis that collecting fMRI data at multiple spatial resolutions may result in improved functional region detection; our simulations in the present paper suggest that this may indeed be the case. We have also shown how a simple decision rule can be applied by practitioners to infer about functional regions given some desired trade off between false positive and false negative errors. This is important because neuroradiologists and neurosurgeons may be more concerned with false negative errors, which could lead to resection of functionally relevant tissue in practice.

With our present work, we propose to base inferences about functional regions on a joint model for images collected at each spatial resolution. Modeling high dimensional correlated outcomes can be quite challenging computationally, and the dataset presented the additional burden of integrating two data sources with different spatial support sets. We circumvented this problem with a Gaussian parent process approximation using only the highest collected resolution image’s voxel locations as a primary support set, and embedding these locations within a larger, toroidal space, leading to

computational gains. As a consequence, our Gaussian process model and related algorithm has very natural extensions to cases with different numbers of data sources. For example, we recognize that not every preoperative plan will rely on collecting both high and standard resolution fMRI data. Our model can easily accommodate the situation where only one spatial resolution is collected by simply dropping unobserved data from the joint outcome.

Just as easily, our model could accommodate data collected at additional spatial resolutions with minimal added computational cost. In fact, in a different setting, we imagine our method could be used for image based meta-analysis to synthesize results from multiple experimental studies. In such a setting, posterior credible sets—Bayesian analogs of spatial confidence sets from [Bowring et al. \(2021\)](#)—could be used to shift inferential focus back to limiting a family wise false positive error rate. With the recent proliferation of large, multi-center imaging collectives (e.g. [Van Horn and Toga, 2009](#)), we feel this may be a promising area for further applied research.

One important limitation of our present model is that we treat both the prior mean model and the errors within each image as stationary processes. In general, stationarity may not be a realistic assumption for imaging data (e.g. [Woolrich et al., 2004](#)). In the case of our mean model, stationarity is only a limitation of the prior: given the data the posterior may still reflect a non-stationary process. In our analysis of the residual images from patient data we found that while there was some residual spatial autocorrelation, this autocorrelation in general decayed to near zero within one to two voxel widths (see the Supplementary Material for figures ([Whiteman et al., 2022](#))). Thus we concluded that prior model mean-field stationarity can lead to reasonable posterior approximations for these data. Our model on the error structure, however, is a bit more restrictive. We further note that residuals tended to show modestly higher dispersion in gray matter than in white (see the Supplementary Material ([Whiteman et al., 2022](#))). While we do not believe this difference is so pronounced as to negatively impact our analyses, it may be worthwhile to explore non-stationary error models. In general, this is a difficult issue. Allowing too much flexibility in the error process may, for example, lead to model non-identifiability or similar complications.

In our simulations and analysis of patient data we showed that our dual resolution method borrows strength from both data sources to improve inference, especially around the edges of active regions, without sacrificing the spatial resolution of the high resolution data (confer from Figs. 7 and 4). To accomplish this task with patient images, we started from the output of typical single subject fMRI analyses, treating summary statistics from voxelwise marginal time series models as data. [Bowman et al. \(2008\)](#) similarly used summary statistics from voxelwise marginal models as data in a group analysis in an experimental setting. Although their approach and setting was different from ours, the authors also chose not to smooth their data during preprocessing and made a similar independent noise approximation in their model likelihood as we do here ([Bowman et al., 2008](#)). We provide additional evaluation of our independent and homogeneous residual noise approximations in the Supplementary Material, and conclude that the approximations are reasonable in our patient data. While we might eventually like to incorporate available time series information into our model, doing so would only add to computational complexity, and it is unclear to what extent spatial inference would improve as a result. At present, a handful of integrated spatiotemporal models have been developed for fMRI studies, but nearly all of these are intended to be fit to single slice data, not whole brain (e.g. [Penny, Trujillo-Barreto and Friston, 2005](#); [Groves, Chappell and Woolrich, 2009](#); [Lindquist, Loh and Yue, 2010](#)). Only more recently have variational approximations been leveraged to enable whole brain spatiotemporal inference at a reasonable computational cost ([Sidén et al., 2017](#)). In its current form, our work uses summaries of temporal data to enable whole brain inference at a very fine spatial scale, but there may be room to incorporate richer temporal information into our model as part of future study.

Finally, in our work we estimated the Gaussian process hyperparameters $\theta = (\tau^2, \psi, \nu)^\top$ from the data in the spirit of empirical Bayes. We accomplished this goal by minimizing a least squares contrast function over an empirical covariogram estimated from the data. Other approaches to learning these parameters include maximizing the data marginal likelihood (e.g. [Mardia and Marshall, 1984](#)),

and fully Bayesian estimation (e.g. [Banerjee et al., 2008](#)). We chose our minimum contrast estimation (MCE) type approach as it is generally more extensible to the size of our dataset. Computing the marginal likelihood would involve inversion of an $(n \times n)$ matrix where n is the number of voxels or spatial locations. Our posterior computation algorithm specifically avoids even constructing such a matrix, which is impossible to store on most computer systems (see section 2.2). Fully Bayesian estimation of θ on the other hand is possible, though still computationally demanding. The kernel bandwidth and exponent parameters, ψ and ν , respectively, can be quite slow to update with multiple data sources, and computation time is a concern in a preoperative setting. In contrast, the partial sill variance τ^2 is straightforward to update in our framework, and an abundance of spatial data make this parameter strongly identifiable. We considered updating τ^2 by default in our algorithm, but found that it did not dramatically affect spatial inference in our data and sometimes led to slower Markov chain mixing. As a result, we decided to condition inference on fixed θ by default in our analyses and consider alternative estimation methods a possibility for future extension.

Conditional on θ , our method enables spatially precise inference on whole brain fMRI data collected at multiple spatial resolutions. Despite the very high dimensional nature of our data, our method is computationally efficient enough to be viable for application in presurgical planning. In addition, we have shown through simulation that inference drawn from a joint model using both available data sources can lead to substantial improvement over inference with single resolution alternatives. We hope that this body of work will benefit the presurgical fMRI community, and may find extension in experimental fields by supporting image based meta analysis and results synthesis.

Appendix A: Details of fMRI data collection and preprocessing

fMRI data collection and methods have been described previously ([Liu et al., 2016](#)). Briefly, the patients were scanned using a 3 Tesla TrioTim scanner (TQ engine, 32 channel head coil; Siemens Medical Solutions, Erlangen) using gradient-echo echo-planar imaging (GE-EPI; 3000 ms repetition time; 30 ms echo time; 0.69 ms echo spacing; GRAPPA acceleration factor 2). High resolution structural T1 weighted MPRAGE and T2 weighted FLAIR scans were also acquired to aid intra-operative neuronavigation and fMRI data preprocessing. The high and standard spatial resolution scans largely followed the same protocols, except that multi-band acceleration was used to increase the spatial resolution of high resolution acquisitions while keeping the temporal resolution the same between protocols (160 volumes were collected for each run).

fMRI time series preprocessing without spatial smoothing was performed prior to our analysis using FSL software (version 6.0.4; [Jenkinson et al., 2012](#)) and the FEAT tool (version 6.00; [Woolrich et al., 2001](#)). Standard resolution fMRI data were padded by 8 voxels in x and y (resulting in a $72 \times 72 \times 48$ grid), and high resolution data by 10 voxels in z (resulting in $120 \times 120 \times 72$ grid). Given standard resolution voxel sizes of $3 \times 3 \times 3.45 \text{ mm}^3$ (patient 1) and $3 \times 3 \times 3.3 \text{ mm}^3$ (patient 2), and high resolution voxel sizes of $1.8 \times 1.8 \times 2.3 \text{ mm}^3$ (patient 1) and $1.8 \times 1.8 \times 2.2 \text{ mm}^3$ (patient 2) this padding ensured that standard and high resolution data spanned the same field-of-view (FoV) within subject prior to further processing. The difference in effective resolution between the two patients resulted only from different interslice gaps (15% for patient 1 vs. 10% for patient 2; interslice gap was lowered for patient 2 because of a smaller head size). Optimal within-subject alignment of the two runs was then achieved by downsampling the volume used as the target reference for motion correction in the high resolution run and supplying this downsampled image as an alternative reference image for motion correction of the standard resolution time series. Per FSL default, we used the middle volume of the recorded frames (the 80th of our 160 volume time series) as the target reference. This volume was downsampled to the gridding of the standard resolution run using FSLeves (part of FSL) using nearest-neighbor interpolation and no additional smoothing.

Data were temporally filtered using a 0.011 Hz high pass filter to remove low frequency drifts, and marginal linear models were fit to the time series data at each voxel to create summary statistic maps of task-related activation. In this last step, task related regressors were convolved with the canonical hemodynamic response function; temporal derivatives of resulting functions were also used as covariates of no interest. Preprocessing resulted in one unsmoothed z -statistic image for each fMRI resolution that summarized task-related activation over the course of the scans. We went on to use the generated test statistic maps as outcome data in our subsequent analysis, treating the contrast images as noisy measures of true activation.

Appendix B: Cavernomas and additional details about Patient 2

Cavernomas are a specific type of arteriovenous malformation without shunting. They contain closely apposed, angiogenetically immature blood vessels, typically with intralesional bleeding residuals. Cavernomas can be treated via microsurgical removal (e.g. Bertalanffy et al., 2002); if left untreated, they may lead to seizures or progressive neurological deficits upon symptomatic micro- or macrohemorrhages. Our patient 2 was found to have a cavernous malformation (cavernoma) with chronic and subacute hemorrhage (Zabramski type I) in her left temporal lobe close to the transverse temporal gyrus and insular cortex.

Acknowledgements

We gratefully acknowledge the indispensable expert technical and collaboration support provided by the MR application and collaboration management teams of Siemens Healthcare GmbH, which enabled us to record multi-band (i.e. simultaneous-multi-slice) -accelerated acquisitions of high-resolution fMRI data at otherwise identical parameter settings like for the standard spatial resolution runs. Dr. Andreas J. Bartsch has additional joint appointments with the Department of Neuroradiology at the University of Wuerzburg, Wuerzburg, Germany; and with the FMRI Centre Department of Clinical Neurology at the University of Oxford, Oxford, United Kingdom. This work was partially supported by NIH R01 DA048993 (Kang and Johnson).

Supplementary Material

Supplement to “Bayesian Inference for Brain Activity from Functional Magnetic Resonance Imaging Collected at Two Spatial Resolutions”

The online supplement to this article provides additional details regarding posterior computation, MCMC and model diagnostics, and comprehensive simulation results.

Source Code Companion to “Bayesian Inference for Brain Activity from Functional Magnetic Resonance Imaging Collected at Two Spatial Resolutions”

C++ programs for analyses presented in this manuscript. High and standard resolution fMRI contrast data for Patient 1 is packaged along with the source code. Software is maintained at <https://github.com/asw221/dualres>.

Posterior computation

In Section 2.3, we outlined a posterior computation algorithm for our model that relies on embedding the covariance of μ_h in a higher dimensional nested block-circulant matrix. We present the details of this algorithm here.

Broadly, our posterior computation algorithm has a Hamiltonian Monte Carlo (HMC) -within-Gibbs sampling structure. Full conditional updates are available for all of our model parameters, but it is numerically challenging to evaluate or sample from the full conditional distribution of μ_h .

In the main text, we discussed how we drew inspiration from the work of Wood and Chan (1994) to design an efficient HMC algorithm to facilitate sampling of $\boldsymbol{\mu}_h$. We elaborate on that algorithm in detail here. First, we embed $\boldsymbol{\mu}_h$ in a higher dimensional random field \boldsymbol{u} , which is constructed so that the prior variance of \boldsymbol{u} is a nested block-circulant matrix \boldsymbol{C} . The prior variance of $\boldsymbol{\mu}_h - \boldsymbol{K}_h$ is a principal submatrix of \boldsymbol{C} (see Fig. 2 in the main text for a schematic picture). We never actually construct or store the full matrix \boldsymbol{C} : its base \boldsymbol{c} can be computed following Algorithm 2 below. With only the base \boldsymbol{c} in memory, the complex eigenvalues of \boldsymbol{C} can be computed using discrete Fourier transform (DFT) software:

$$\boldsymbol{\lambda} \leftarrow \mathcal{F}(\boldsymbol{c})/N,$$

where N is the number of elements in \boldsymbol{c} .

Then, let $\boldsymbol{\xi} = \boldsymbol{u} + \boldsymbol{v}i$ represent a complex Gaussian random field with real part \boldsymbol{u} , imaginary part \boldsymbol{v} , and with the prior properties that $\boldsymbol{u} \perp \boldsymbol{v}$ and $\text{var}(\boldsymbol{u}) \equiv \text{var}(\boldsymbol{v}) \equiv \boldsymbol{C}$. Writing out the prior in terms of $\boldsymbol{\xi}$,

$$\boldsymbol{\xi} = \boldsymbol{u} + \boldsymbol{v}i, \quad \boldsymbol{u} \sim \mathcal{N}(\mathbf{0}, \boldsymbol{C}), \quad \boldsymbol{v} \sim \mathcal{N}(\mathbf{0}, \boldsymbol{C}),$$

does not change our model, moreover: the imaginary and non-brain parts of $\boldsymbol{\xi}$ can simply be integrated away to recover our original prior on $\boldsymbol{\mu}_h$. Similarly, our plan will be to obtain posterior samples of $\boldsymbol{\xi}$ through HMC, and then simply discard extraneous elements to be left with a posterior sample of $\boldsymbol{\mu}_h$.

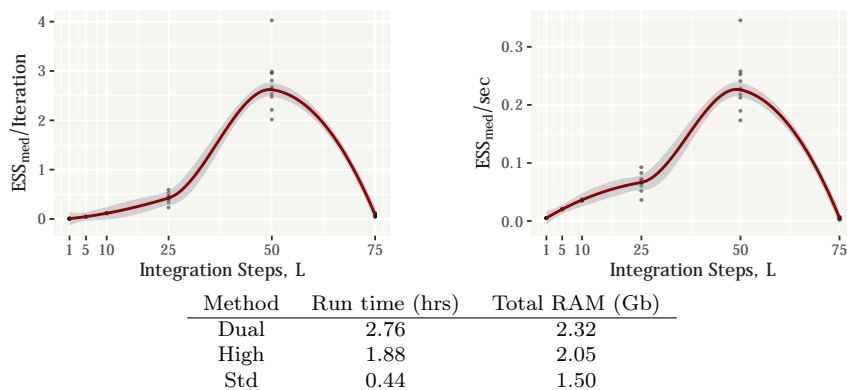


Fig 9: Dual resolution algorithm efficiency (median ESS per iteration and per second) as a function of integration steps L in analysis of whole brain patient data. ESS denotes the effective sample size of elements of $\boldsymbol{\mu}_h$. Peak efficiency was estimated around $L = 50$. Analyses were replicated 10 times for each value of L , and were timed on a Thelio System76 desktop with 62 Gb of free RAM and 20 logical cores (3.3 GHz Intel[®] Core[™] i9 processors). Below the figure, we summarize the overall computational burden for real patient data on this hardware and at $L = 25$ steps. Run time is given in hours per 1,000 iterations; our naive method has the same cost as the high-resolution only method.

HMC relies on several tuning parameters, including the choice of momentum distribution, mass matrix, step size, and number of numerical integration steps (Neal, 2011). While a review of HMC-flavored algorithms and tuning parameter selection is beyond the scope of this paper, we will detail our approach to tuning parameter selection for model (1). Given the other tuning parameters and a target Metropolis-Hastings rate (which we fixed at 65%), we tuned the step size ϵ during warm up following the dual averaging method of Hoffman and Gelman (2014). We then fixed ϵ_0 at the value of ϵ on the last burnin iteration, and drew $\epsilon \sim \text{Uniform}(0.9 \epsilon_0, 1.1 \epsilon_0)$ to induce random integration path lengths (the product ϵL) during sampling, potentially helping the algorithm escape local

modes (Neal, 2011). To inform selection of the number of leapfrog integration steps L , we performed repeated analyses of patient data. Results of this experiment suggest $L = 25$ or $L = 50$ as practical starting points for best algorithmic efficiency (see Fig. 9).

Let,

$$\mathcal{L}(\boldsymbol{\xi}) = \ln \pi(\boldsymbol{\xi} \mid \mathbf{Y}_h, \mathbf{Y}_s, \boldsymbol{\mu}_s, \boldsymbol{\theta}, \sigma_h^2, \sigma_s^2, r)$$

represent the full conditional log posterior of $\boldsymbol{\xi}$. Since $\exp\{\mathcal{L}(\boldsymbol{\xi})\}$ is complex Gaussian, we in turn chose a complex Gaussian distribution for HMC momenta. Girolami and Calderhead (2011) suggest exploiting Riemannian geometry in HMC by adapting the algorithm’s mass matrix, \mathbf{M} , to the local curvature of the log posterior. The authors suggest that taking \mathbf{M} proportional to the negative Hessian of the log posterior leads to improved algorithmic efficiency in high dimensions, though this approach is not typically feasible when the dimension of \mathbf{M} is more than a few thousand. Up to a permutation of $\boldsymbol{\xi}$, in our model, we have that,

$$-\nabla^2 \mathcal{L}(\boldsymbol{\xi}) = \begin{pmatrix} \sigma_h^{-2} \mathbf{I} + \sigma_s^{-2} \mathbf{W}^T \mathbf{W} \\ \mathbf{0} \end{pmatrix} + \mathbf{F} \boldsymbol{\Lambda}^{-1} \mathbf{F}^H, \quad (10)$$

where $\boldsymbol{\Lambda} = \text{diag}(\boldsymbol{\lambda})$, and \mathbf{F} is the 3D DFT matrix as in the main text. In the present case, (10) is ultrahigh dimensional and impossible to work with directly, but by dropping the term involving $\mathbf{W}^T \mathbf{W}$, which is dense, and extending $\sigma_h^{-2} \mathbf{I}$ we can arrive at an alternative choice of mass matrix. Let $\mathbf{M}(\sigma_h^2)$ denote the matrix-valued function,

$$\mathbf{M}(\sigma_h^2) = \mathbf{F}[\boldsymbol{\Lambda}^{-1} + \sigma_h^{-2} \mathbf{I}] \mathbf{F}^H, \quad (11)$$

which, like \mathbf{C} , is nested block-circulant, and easy to compute with. Circulant matrices have been used successfully as preconditioners in other gradient-based optimization schemes for imaging problems (e.g. Fessler and Booth, 1999). If each element in $\text{Re}(\boldsymbol{\lambda})$ is strictly greater than zero, $\mathbf{M}(\sigma_h^2)$ is positive definite and so can be used to define a metric tensor on a Riemannian manifold as in Girolami and Calderhead (2011). Some additional intuition can be gained by considering how (10) relates to a missing data problem. If we were only modeling high resolution data, and those data were observed on the entire extended grid with variance σ_h^2 , then (11) would be exactly the negative Hessian of $\mathcal{L}(\boldsymbol{\xi})$.

Algorithm 1 Riemann manifold HMC for dual resolution mapping models. \mathbf{F} denotes the scaled 3D DFT matrix; products of the form, $\mathbf{F}^H \mathbf{p} = \mathcal{F}^{-1}(\mathbf{p})$, for example, can be computed efficiently using DFT software.

```

1: procedure UPDATEMEAN( $\boldsymbol{\xi}; \boldsymbol{\lambda}, \sigma_h^2, \epsilon, L$ )
2:   Compute eigenvalues of  $\mathbf{M}(\sigma_h^2)$ :
3:      $\lambda_i^M \leftarrow \sigma_h^{-2} + \lambda_i^{-1}$ 
4:     Set  $\boldsymbol{\Lambda}_M \leftarrow \text{diag}\{\lambda_i^M\}, i = 1, \dots, \text{dim}(\boldsymbol{\xi})$ 
5:   Sample momentum,  $\mathbf{p} \sim \mathcal{CN}(\mathbf{0}, \mathbf{F} \boldsymbol{\Lambda}_M \mathbf{F}^H)$ 
6:   Compute total energy,  $H \leftarrow -\mathcal{L}(\boldsymbol{\xi}) + \frac{1}{2} \mathbf{p}^H \mathbf{F} \boldsymbol{\Lambda}_M^{-1} \mathbf{F}^H \mathbf{p}$ 
7:   Set  $\boldsymbol{\xi}^{\text{new}} \leftarrow \boldsymbol{\xi}$ 
8:   for  $l$  in  $1, \dots, L$  do ▷ Leapfrog integrator
9:      $\mathbf{p} \leftarrow \mathbf{p} + \frac{\epsilon}{2} \nabla \mathcal{L}(\boldsymbol{\xi}^{\text{new}})$ 
10:     $\boldsymbol{\xi}^{\text{new}} \leftarrow \boldsymbol{\xi}^{\text{new}} + \epsilon \mathbf{F} \boldsymbol{\Lambda}_M^{-1} \mathbf{F}^H \mathbf{p}$ 
11:     $\mathbf{p} \leftarrow \mathbf{p} + \frac{\epsilon}{2} \nabla \mathcal{L}(\boldsymbol{\xi}^{\text{new}})$ 
12:   Compute  $H^{\text{new}} \leftarrow -\mathcal{L}(\boldsymbol{\xi}^{\text{new}}) + \frac{1}{2} \mathbf{p}^H \mathbf{F} \boldsymbol{\Lambda}_M^{-1} \mathbf{F}^H \mathbf{p}$ 
13:   Set  $\boldsymbol{\xi} \leftarrow \boldsymbol{\xi}^{\text{new}}$  with probability  $\alpha = \min\{1, \exp(H - H^{\text{new}})\}$ 
14:   Discard all elements of  $\boldsymbol{\xi}$  that do not correspond to  $\boldsymbol{\mu}_h$ 
15:   Return posterior sample of  $\boldsymbol{\mu}_h$ 

```

With all this in hand, samples of $\boldsymbol{\mu}_h$ can be drawn following Algorithm 1. In particular, note how all products involving \mathbf{F} can be computed with DFT software. In addition, the quadratic forms in

Algorithm 1 represent computations over ultrahigh dimensional components. The quadratic form $\mathbf{p}^H \mathbf{F} \Lambda_M^{-1} \mathbf{F}^H \mathbf{p}$, for example, can be evaluated by computing,

$$\phi \leftarrow \mathcal{F}^{-1}(\mathbf{p}),$$

into a temporary product, ϕ , and then summing over terms $\sum_i \bar{\phi}_i \cdot \phi_i / \lambda_i^M$, where \bar{a} denotes the complex conjugate of a . When working in single precision, we found it necessary to use the Kahan summation algorithm (Kahan, 1965), or similar correction, to evaluate these long sums accurately.

Finally, our other parameters, μ_s , σ_h^2 , and σ_s^2 can easily be sampled with full conditional Gibbs updates. We particularly note that our prior places the restriction $\sigma_h^2 > \sigma_s^2$ so that the conditional posteriors of both nugget variance parameters are truncated inverse Gamma. We sometimes encountered numerical difficulty sampling these parameters during warm up. As a result, we chose to ignore the restriction on σ_h^2 and σ_s^2 programmatically, and simply discard posterior samples where the restriction was not satisfied. After warm up, however, we found that even when working with patient data the posterior probability that $\sigma_h^2 > \sigma_s^2$ was effectively unity, and that we never had to discard or post-process MCMC samples in this way.

Circulant base construction

This section presents a simple algorithm to illustrate circulant matrix base computation for our applications.

Algorithm 2 Compute the base of a circulant matrix associated with a 3D grid

```

1: procedure COMPUTECIRCULANTBASE( $\mathbf{d}$ ,  $K(\cdot, \cdot; \theta)$ )
2:   Inputs:  $\mathbf{d}$ , original 3D grid dimensions;  $K(\cdot, \cdot; \theta)$  covariance function parameterized by  $\theta$ 
3:   Compute extended grid dimensions,  $d_i^* \leftarrow 2^{\lceil \log_2 [2^{d_i-1}] \rceil}$  for  $i = 1, 2, 3$ 
4:    $k \leftarrow 0$ ,  $h \leftarrow 1$ 
5:   Find location  $\mathbf{v}_1$  associated with grid position (1, 1, 1)
6:   for  $l$  in  $1, \dots, d_3^*$  do ▷ Column-major order
7:      $j \leftarrow 0$ 
8:     if  $l \leq d_3$  then  $k \leftarrow k + 1$  else  $k \leftarrow k - 1$ 
9:     for  $m$  in  $1, \dots, d_2^*$  do
10:       $i \leftarrow 0$ 
11:      if  $m \leq d_2$  then  $j \leftarrow j + 1$  else  $j \leftarrow j - 1$ 
12:      for  $n$  in  $1, \dots, d_1^*$  do
13:        if  $n \leq d_1$  then  $i \leftarrow i + 1$  else  $i \leftarrow i - 1$ 
14:        Find location  $\mathbf{v}$  associated with grid position ( $i, j, k$ )
15:        Compute  $c_h \leftarrow K(\mathbf{v}_1, \mathbf{v}; \theta)$ 
16:         $h \leftarrow h + 1$ 
17:   Return circulant matrix base,  $\mathbf{c}$ 

```

Analysis of patient 1 data: Model diagnostics

In this section we include several of the general attempts we have made to probe Markov chain convergence and model fit in our analysis of patient data.

As discussed in the main text, Fig. 10 shows trace plots for three chains of Hamiltonian Monte Carlo (HMC) draws of the mean parameter for six random voxels. In all cases we examined, chains appear to show good convergence and mixing. Fig. 11 (*left*) shows empirical covariograms and estimated covariance functions for residual images from each method. We found that the estimated residual correlation functions' full widths at half maxima were on the order of the minimum voxel dimensions in all cases. These analyses suggested that residual correlation decayed to near zero within the smallest voxel dimension widths, leading us to conclude that residual independence was a reasonable approximation in our data.

The right panel of Fig. 11 shows histograms of the residuals from our dual resolution method roughly separated by gross tissue type. We chose to parse the residuals in this way due to some concern that a homogeneous residual variance approximation may not be fully justifiable across the

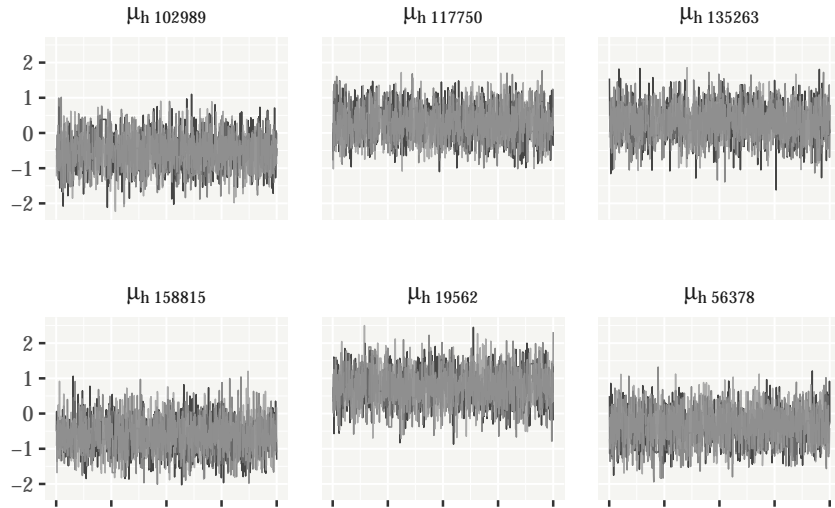


Fig 10: Trace plots for the mean parameter of six random voxels from analysis of patient 1's data with our dual resolution model. Three different HMC chains are overlaid on one another in each subfigure.

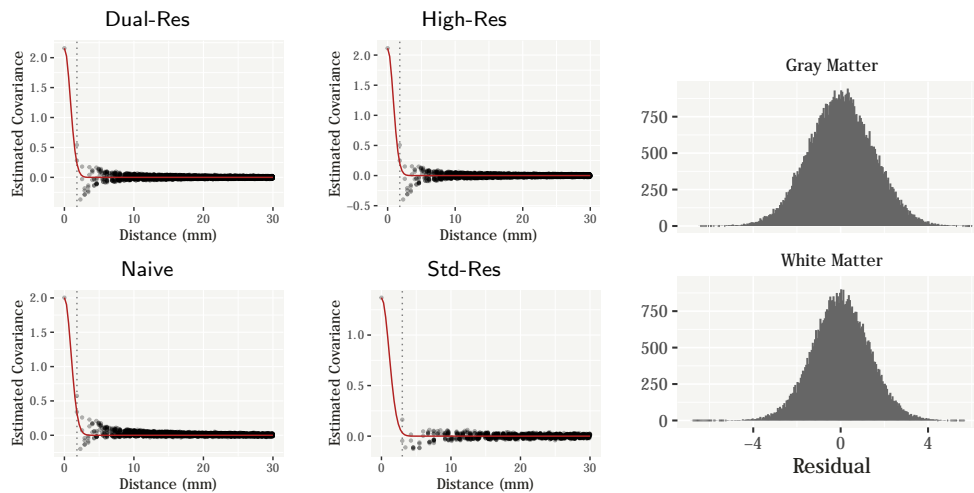


Fig 11: (*Left*) Residual covariograms for each method. The dotted lines show minimum voxel dimensions for each resolution, suggesting that the residual independence approximation is reasonable in these data. (*Right*) Dual resolution method residual histograms roughly separated by gross tissue type. Residuals have modestly higher dispersion in gray matter than in white.

whole brain. To construct this figure, we created non-overlapping gray and white matter tissue labels using the FAST program from the FSL software suite (Zhang, Brady and Smith, 2001), though the presence of the tumor complicates this procedure. The figure suggests that residuals had modestly higher dispersion in gray matter (standard deviation = 1.49) than in white (standard deviation = 1.31). If it were not for the tumor, we might ideally only want to analyze gray matter voxels for signs of task-related activation. Given the present context, however, this strategy is not completely

possible. As it stands, although it appears homogeneous residual variance may not strictly hold across different tissue types, we do not believe the approximation is so poor as to grossly impact our analyses in a negative way.

We further examined posterior predictive distributions for the data from each voxel in the high resolution image, and compared the distributions against the observed data (analysis not shown). Dual resolution model posterior predictive inverse quantiles for the observed data were roughly uniform, suggesting that data outliers occurred no more or less frequently than would be expected given the model.

Analysis of patient 2 data: Sensitivity analysis

In this section we include a brief sensitivity analyses related to the choice of neighborhood size and covariance function in our dual resolution method.

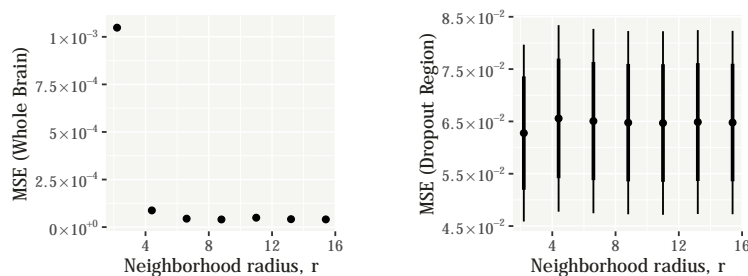


Fig 12: Mean squared error (MSE) of the posterior expectation of $\mu(\cdot)$ given fixed θ but different values of r . The (*left*) panel shows MSE of $\mu(\cdot)$ evaluated across the whole brain, while the (*right*) panel shows the predictive MSE for voxels in patient 2’s dropout region. Thick and thin lines give approximate 80% and 95% confidence intervals.

Our dual resolution mapping method relies on a neighborhood radius parameter r to construct locally kriged samples of μ_s given μ_h (see section 2.2 in the main text). Conceptually, this construction is somewhat inspired by the so called nearest neighbor Gaussian process (Datta et al., 2016; Finley et al., 2019). In practice, we treat r as a hyperparameter and condition analyses on it, though it is of interest to understand how the choice of r affects inference about μ_h . In our patient data analyses (sections 4.2 and 4.3 in the main text), we set r to be approximately equal to the estimated full kernel width at half maximum. This resulted in neighborhood sizes on the order of 300–700 voxels for our patient data.

To explore the influence of r on estimation and prediction, we fit our dual resolution model to the patient 2 data under several different settings, all for fixed θ . As a comparison point, we took the posterior mean of $\mu(\cdot)$ fit to the data without missingness and conditioned on $r = 11$ mm. We then compared against the posterior mean of $\mu(\cdot)$ from repeat analyses of the with-missingness data and varying values of r (see section 4.3 in the main text for an explanation of the two data sets). For these repeat analyses, we chose values of r based on multiples of the largest high resolution image voxel dimension (2.2 mm). Fig. 12 summarizes this experiment in terms of the squared error of $\mu(\cdot)$ averaged over the whole brain (*left*) and voxels in the dropout region (*right*). From these results we conclude that as long as r is sufficiently large (≥ 6.6 mm or so; corresponding to neighborhood sizes of at least 100–200 voxels), it does not appear to have much influence on posterior estimates.

A reviewer pointed out that, especially in our analysis of Patient 2’s covariogram, the exponential model we used tends to underestimate the proximal empirical covariances. We chose to use the radial basis covariance function-family largely because of the substantial history of gaussian smoothing in applied MRI analysis. Additional literature suggests exponential smoothing kernels are perhaps more appropriate for fMRI data (Groves, Chappell and Woolrich, 2009). The reviewer’s

note prompted us to consider alternative covariance functions and their impact on our analysis, and we summarize one alternative here.

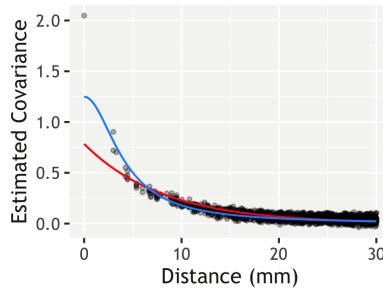


Fig 13: Reanalysis of Patient 2’s covariogram. The red line reproduces the exponential covariance model from the main text; the blue line shows a rational quadratic covariance model.

In Fig. 13, we compare the exponential covariance model from the main text against a rational quadratic model, and find that the rational quadratic model fits the proximal empirical covariances quite well. The specific rational quadratic model in the above figure is,

$$k_{R.Q.}(\mathbf{v}, \mathbf{v}') = 1.25 \left(1 + \frac{\|\mathbf{v} - \mathbf{v}'\|^2}{16.67 \times 0.99} \right)^{-0.99}.$$

It is impossible to tell visually, but the rational quadratic model in Fig. 13 is *sub-optimal* in the sense that it has a very slightly higher residual weighted sum of squares than the exponential model. Better than either might be some weighted linear or piecewise combination of the two.

Choice of the covariance function is more art than science. An interesting feature of this problem is that the empirical covariances will tend to overestimate the true mean field covariance if the noise is positively correlated spatially. Assuming as we do in the main text that $Y(\mathbf{v}) = \mu(\mathbf{v}) + \epsilon(\mathbf{v})$ and that $\mu(\mathbf{v}) \perp \epsilon(\mathbf{v}')$ for all \mathbf{v}, \mathbf{v}' , the empirical covariances will be overestimates since,

$$\text{cov}\{Y(\mathbf{v}), Y(\mathbf{v}')\} = \text{cov}\{\mu(\mathbf{v}), \mu(\mathbf{v}')\} + \text{cov}\{\epsilon(\mathbf{v}), \epsilon(\mathbf{v}')\}.$$

Although in our work we modeled the error structure as a white noise-type process for simplicity, it is perhaps more realistic to assume the errors may be positively correlated over short distances. If the errors are in fact correlated spatially, then it may be preferable to use a covariance model that underestimates the proximal empirical covariances.

In practice we observed mild, intermittent spatial autocorrelation patterns in our residual images (see Section 5 for example). We switched from the exponential to the rational quadratic covariance function and did not find that this change ameliorated residual autocorrelation patterns. Because the rational quadratic covariance model places higher correlation between proximal elements and decays more rapidly, we found that it yielded posterior inference that was both noisier and less sensitive than our primary analysis (see Fig. 14). Clearly results are sensitive to the choice of covariance function to some degree, underscoring the importance of these issues.

2D simulation results

In this section we give results designed augment those reported in section 3.2 with additional simulation settings. Tables follow the exact format of Table 1 in the main text.

In all cases considered, our dual resolution method had the lowest mean squared error (MSE) and false negative rate. Of potential interest, however, is that the high resolution-only method was the second best performer when data were simulated with a marginal exponential correlation structure

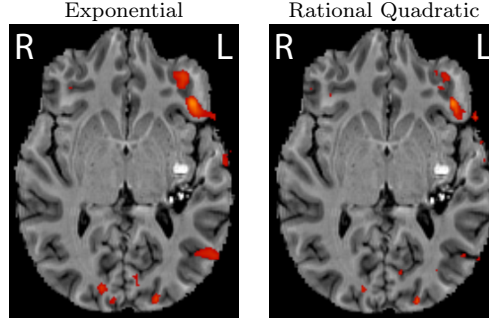


Fig 14: The figure shows thresholded posterior inference of activation regions for Patient 2 in an example horizontal slice. The color scale is shared between sub figures and reflects an approximate posterior probability of activation (range 0.3–1.0).

(Table 2), and the naive data averaging method was the second best performer when data were simulated with a marginal Gaussian correlation structure (Table 3).

Covariance function estimation

In this section we detail our procedure to estimate isotropic covariance functions from 3D data; in practice the method could be extended to arbitrary n dimensional data sources. The methods considered herein are not new but are included for completeness. We also report simulation results using this method to estimate the covariance from small three dimensional images and show that the method has relatively small bias in most simulation settings.

Algorithm 3 Minimum contrast estimation of θ : high level overview

- 1: **procedure** ESTIMATEIMAGECOVARIANCE(\mathbf{Y} , $k(\cdot; \theta)$, Θ) \triangleright With the argument to $k(\cdot; \theta)$ the Euclidean distance between any two points, $\|\mathbf{v} - \mathbf{v}'\|$
 - 2: Inputs: Image \mathbf{Y} ; covariance function $k(\cdot; \theta)$ parameterized by θ with feasible region Θ
 - 3: Construct $\mathcal{D} \leftarrow \text{EXTRACTCOVARIANCESUMMARY}(\mathbf{Y})$ \triangleright With $\mathcal{D} = (\mathbf{d}, \hat{\mathbf{c}}, \boldsymbol{\omega})$
 - 4: Return $\arg \min_{\theta \in \Theta} \sum_{i=1}^{\dim(\hat{\mathbf{c}})} \omega_i [\hat{c}_i - k(d_i; \theta)]^2$
-

Algorithm 3 outlines our minimum contrast estimation (MCE) procedure at a high level. The algorithm first extracts summary data $\mathcal{D} = (\mathbf{d}, \hat{\mathbf{c}}, \boldsymbol{\omega})$ from the input data source \mathbf{Y} , where $\hat{\mathbf{c}}$ are empirical covariances between elements of \mathbf{Y} offset by corresponding distances \mathbf{d} , and $\boldsymbol{\omega}$ is a set of corresponding weights (defined below in algorithm 4). The algorithm then finds θ from within constraint region Θ to minimize a weighted least squares contrast between the \hat{c}_i and $k(d_i; \theta)$.

With $k(\cdot; \theta)$ taken to be the radial basis function as in (5), for example, the parameters θ correspond to the marginal variance τ^2 , correlation bandwidth ψ , and exponent ν . For this problem, we took the feasible region Θ to constrain $0 < \tau^2 < \hat{c}_0$, $0 < \psi$, and $0 < \nu \leq 2$, where \hat{c}_0 is the empirical variance of \mathbf{Y} . For problems we consider, we found that the additional constraint $\psi \leq \nu$ frequently helped improve estimation.

Construction of \mathcal{D} using a modified 3D raster scan is outlined in algorithm 4. In the algorithm, empirical covariances between voxels and their neighbors are computed by shifting the (i, j, k) index of each voxel by the rows of the matrix \mathbf{P} (which is constructed with the procedure outlined in Algorithm 5). The rows of \mathbf{P} define a series of perturbations in a dense 3D raster scan. In one dimension, a raster scan might only look ahead one pixel at a time so as to visit each pair of adjacent pixels only once. In two dimensions, the procedure might be defined to look ahead one pixel and look down one pixel for the same reason. In three dimensions, a simple raster might look ahead, down, and to the right by one or more voxels. We designed our procedure to sample local

<i>Model</i>	<i>Kernel</i>	$SNR_s:SNR_h$	SNR_h	<i>MSE</i>	<i>False –</i>
Dual	Exponential	1	0.1	0.20	31.8% (0.4)
High	Exponential	1	0.1	0.23	34.0% (0.5)
Naive	Exponential	1	0.1	0.30	43.6% (0.4)
Std	Exponential	1	0.1	0.47	43.1% (0.6)
Dual	Exponential	1	0.2	0.17	29.3% (0.4)
High	Exponential	1	0.2	0.20	31.0% (0.4)
Naive	Exponential	1	0.2	0.29	43.0% (0.3)
Std	Exponential	1	0.2	0.43	40.6% (0.4)
Dual	Exponential	2	0.1	0.18	30.6% (0.4)
High	Exponential	2	0.1	0.23	34.0% (0.5)
Naive	Exponential	2	0.1	0.29	42.7% (0.4)
Std	Exponential	2	0.1	0.43	40.6% (0.4)
Dual	Exponential	2	0.2	0.15	28.5% (0.3)
High	Exponential	2	0.2	0.20	31.0% (0.4)
Naive	Exponential	2	0.2	0.29	42.4% (0.3)
Std	Exponential	2	0.2	0.41	40.5% (0.3)
Dual	Exponential	4	0.1	0.16	29.5% (0.3)
High	Exponential	4	0.1	0.23	34.0% (0.5)
Naive	Exponential	4	0.1	0.29	42.3% (0.3)
Std	Exponential	4	0.1	0.41	40.5% (0.3)
Dual	Exponential	4	0.2	0.14	27.9% (0.3)
High	Exponential	4	0.2	0.20	31.0% (0.4)
Naive	Exponential	4	0.2	0.28	42.1% (0.3)
Std	Exponential	4	0.2	0.40	40.8% (0.3)

TABLE 2

Results for estimation and inference quality in 2D simulations when background signal has an Exponential correlation structure. As in Table 1, results for the High resolution method do not change across the different SNR ratios, but are repeated to facilitate comparison. MSE refers to mean squared error computed over the entire high resolution mean parameter vector. False – reports the mean (SE) false negative error rate when the number of discoveries was fixed at 450. One hundred replicates per parameter combination.

pairs of voxels more densely than this while still only visiting each unique pair once. Briefly, our algorithm “looks ahead” by visiting pairs of voxels within an $(n_0 \times n_0 \times n_0)$ voxel cube such that the polar and azimuthal angles of the search are between $[0^\circ, 180^\circ)$. We further extended this search by adding simple raster scan perturbations out to an n_1 voxel distance. In algorithm 5, we defined $n_0 = 18$ voxels and $n_1 = 25$ voxels by default. Our default values encompass a large number of perturbations while limiting the total computation time to a few seconds for full scale brain images.

Model	Kernel	$SNR_s:SNR_h$	SNR_h	MSE	False –
Dual	Gaussian	1	0.1	0.24	29.8% (0.3)
High	Gaussian	1	0.1	0.28	34.1% (0.3)
Naive	Gaussian	1	0.1	0.25	34.5% (0.3)
Std	Gaussian	1	0.1	0.59	50.0% (0.4)
Dual	Gaussian	1	0.2	0.17	24.2% (0.2)
High	Gaussian	1	0.2	0.21	27.1% (0.2)
Naive	Gaussian	1	0.2	0.19	27.1% (0.2)
Std	Gaussian	1	0.2	0.58	43.5% (0.3)
Dual	Gaussian	2	0.1	0.21	27.5% (0.2)
High	Gaussian	2	0.1	0.28	34.1% (0.3)
Naive	Gaussian	2	0.1	0.24	33.3% (0.3)
Std	Gaussian	2	0.1	0.58	43.5% (0.3)
Dual	Gaussian	2	0.2	0.15	22.8% (0.2)
High	Gaussian	2	0.2	0.21	27.1% (0.2)
Naive	Gaussian	2	0.2	0.18	26.4% (0.2)
Std	Gaussian	2	0.2	0.57	38.6% (0.2)
Dual	Gaussian	4	0.1	0.18	25.0% (0.2)
High	Gaussian	4	0.1	0.28	34.1% (0.3)
Naive	Gaussian	4	0.1	0.24	33.0% (0.3)
Std	Gaussian	4	0.1	0.57	38.6% (0.2)
Dual	Gaussian	4	0.2	0.12	21.1% (0.2)
High	Gaussian	4	0.2	0.21	27.1% (0.2)
Naive	Gaussian	4	0.2	0.18	25.9% (0.2)
Std	Gaussian	4	0.2	0.54	34.8% (0.2)

TABLE 3

Results for estimation and inference quality in 2D simulations when background signal has a Gaussian correlation structure. As in Tables 1 and 2, results for the High resolution method do not change across the different SNR ratios, but are repeated to facilitate comparison. MSE refers to mean squared error computed over the entire high resolution mean parameter vector. False – reports the mean (SE) false negative error rate when the number of discoveries was fixed at 450. One hundred replicates per parameter combination.

Algorithm 4 Compute empirical covariance summary data

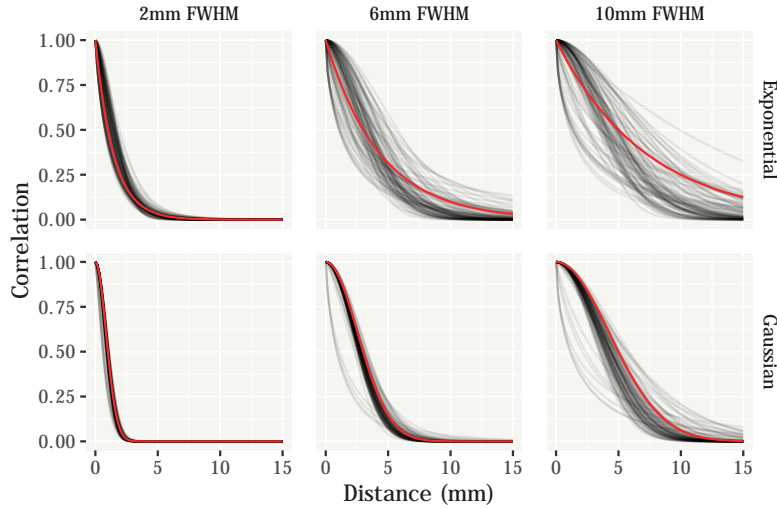
```

1: procedure EXTRACTCOVARIANCESUMMARY( $\mathbf{Y}$ ,  $n_0$ ,  $n_1$ )
2:   Inputs: Image  $\mathbf{Y}$  with dimensions  $\mathbf{q} \in \mathbb{R}^3$ . We set  $n_0 = 18$ , and  $n_1 = 25$  by default
3:   Set  $N \leftarrow q_1 \cdot q_2 \cdot q_3$  ▷  $N$  is the total number of voxels in image  $\mathbf{Y}$ 
4:   Store  $\mathbf{P} \leftarrow \text{IMAGESCANPERTURBATIONS}(n_0, n_1)$  ▷  $\mathbf{P}$  is an  $(M \times 3)$  matrix of integers
5:   Allocate  $\mathbf{d} \in \mathbb{R}^M$ ,  $\hat{\mathbf{c}} \in \mathbb{R}^M$  ▷  $\mathbf{d}$ —perturbation distances;  $\hat{\mathbf{c}}$ —empirical covariances
6:    $\mathbf{s}^{ab} \leftarrow \mathbf{0}_M$ ,  $\mathbf{s}^a \leftarrow \mathbf{0}_M$ ,  $\mathbf{s}^b \leftarrow \mathbf{0}_M$  ▷ Accumulators for sufficient statistics
7:    $\mathbf{r} \leftarrow \mathbf{0}_M$  ▷ Accumulators for counts of voxel pairs
8:   Compute sufficient statistics for pairs of voxels separated by perturbation distances:
9:   for  $h$  in  $1, \dots, N$  do ▷ Outer loop over voxels
10:    Locate grid position  $(i, j, k)$  such that corresponds to voxel  $\mathbf{v}_h$ 
11:    if  $Y_{ijk}$  corresponds to brain data then
12:      for  $m$  in  $1, \dots, M$  do ▷ Inner loop over perturbations
13:         $(i', j', k') \leftarrow (i, j, k) + \mathbf{P}_m^T$ 
14:        if  $Y_{i'j'k'}$  corresponds to brain data then ▷ Update sufficient statistics
15:           $s_m^{ab} \leftarrow s_m^{ab} + Y_{ijk} \cdot Y_{i'j'k'}$ 
16:           $s_m^a \leftarrow s_m^a + Y_{ijk}$ ;  $s_m^b \leftarrow s_m^b + Y_{i'j'k'}$ 
17:           $r_m \leftarrow r_m + 1$ 
18:   Compute distances and empirical covariances associated with grid perturbations:
19:   “Locate” voxel  $\mathbf{v}_0$  associated with grid position  $(i, j, k) = \mathbf{0}_3$ 
20:   for  $m$  in  $1, \dots, M$  do
21:     “Locate” voxel  $\mathbf{v}'$  associated with grid position  $\mathbf{P}_m$ 
22:      $d_m \leftarrow \|\mathbf{v}_0 - \mathbf{v}'\|$ 
23:     if  $r_m > 1$  then
24:        $\hat{\mathbf{c}}_m \leftarrow (s_m^{ab} - s_m^a s_m^b / r_m) / (r_m - 1)$ 
25:   Set  $\omega_m \leftarrow \#(\mathbf{d} = d_m)$  for  $m$  in  $1, \dots, M$  ▷ Count of instances of unique elements in  $\mathbf{d}$ 
26:   Set  $\omega_m \leftarrow 1/\omega_m$  if  $\omega_m > 0$  and  $\omega_m \leftarrow 0$  otherwise for  $m$  in  $1, \dots, M$ 
27:   Return  $\mathcal{D} = (\mathbf{d}, \hat{\mathbf{c}}, \boldsymbol{\omega})$ 

```

Algorithm 5 Construct matrix \mathbf{P} of grid index perturbations for minimum contrast estimation procedure.

- 1: **procedure** IMAGESCANPERTURBATIONS(n_0, n_1)
 - 2: Inputs: positive integers $n_0, n_1, n_0 < n_1$
 - 3: Construct principal direction matrix $\mathbf{U} \in \mathbb{R}^{(14 \times 3)}$ such that each element $U_{ij} \in \{-1, 0, 1\}$; the polar angle of each row of \mathbf{U} is between $[0^\circ, 180^\circ)$; and the azimuthal angle of each row of \mathbf{U} is between $[0^\circ, 180^\circ)$. In our construction, \mathbf{U} includes a row of all 0's
 - 4: Construct $\mathbf{Q} \in \mathbb{R}^{(n_0^3 \times 3)}$ with rows consisting of all 3-element permutations of elements of $(1, \dots, n_0)$
 - 5: Compute $\mathbf{P} \leftarrow \mathbf{Q} * \mathbf{U}$, where $*$ denotes the column-wise Khatri-Rao product
 - 6: **for** k in $n_0 + 1, \dots, n_1$ **do**
 - 7: $\mathbf{P} \leftarrow [\mathbf{P}^\top \ k \mathbf{I}_3]^\top$
 - 8: Remove duplicate rows from \mathbf{P}
 - 9: Return \mathbf{P}
-



<i>Kernel</i>	<i>FWHM</i>	<i>Bias</i>	<i>Variance</i>
Exponential	2	-6.73×10^{-3}	8.46×10^{-4}
Exponential	6	-6.04×10^{-2}	7.22×10^{-3}
Exponential	10	-1.47×10^{-1}	1.56×10^{-2}
Gaussian	2	6.70×10^{-3}	1.17×10^{-3}
Gaussian	6	-3.86×10^{-3}	3.45×10^{-3}
Gaussian	10	-3.07×10^{-2}	1.73×10^{-2}

Fig 15: Recovery of the correlation function in small 3D images. Each gray line shows a correlation function estimated in repeated simulation (true correlation functions for each panel shown in red). In the table, *Bias* and *Variance* were computed pointwise and averaged over a dense grid from $[0, 15]$ (mm).

Fig. 15 presents the results of a simulation assessing the performance of our MCE procedure. We simulated small 3D images on a $(32 \times 32 \times 16)$ grid, treating voxels as isotropic 1 mm^3 . In our simulation, we drew mean images from Gaussian processes with either Exponential or Gaussian correlation functions; unit marginal variance; and either two, six, or ten mm full widths at half maxima. Mean images were corrupted with independent Gaussian noise with the signal to noise ratio set to 0.2 roughly to match our observed patient data and our 2D simulations in section 3.

Since the Gaussian predictive process basis described in section 2.2 relies only on the correlation bandwidth and exponent parameters ψ and ν , the most important measure of estimation success in our setting is recovery of the correlation function, not necessarily estimation of θ itself. For

any given dataset, the nonlinear least squares objective in algorithm 3 might be multimodal in θ , but this is relatively unimportant if the resulting correlation functions at different modes behave similarly.

In Fig. 15, the red line in each panel shows the true correlation function used to generate underlying mean images in simulation, and the corresponding gray lines show estimated correlation functions from 100 repeated simulations. The table below the panels summarizes pointwise bias and variance averaged over a grid of 1,000 equally spaced points from $[0, 15]$ (mm). In the worst case scenario (10 mm FWHM Exponential correlation function), pointwise mean squared error was on average only about 3.8×10^{-2} , and was between $[1.1, 7.5] \times 10^{-2}$ for 95% of points on the grid. Even with relatively small 3D images, these results suggest our MCE procedure can recover the true correlation functions reasonably well.

Symmetry of our custom covariance function

A remark on the cross covariance between $\mu(B_h)$ and $\mu(B_s)$ in our dual resolution mapping prior.

In the main body text, we defined a custom covariance function to help map between high and standard spatial resolution images. We reproduce that covariance function here for convenience:

$$K(\mathbf{v}, \mathbf{v}') = \begin{cases} k(\mathbf{v}, \mathbf{v}') & \text{if } \mathbf{v}' \in B_h \\ w^\top(\mathbf{v})k(B_h, \mathbf{v}') & \text{otherwise,} \end{cases}$$

where $w(\cdot) \approx K(B_h, B_h)^{-1}k(B_h, \cdot)$ (equations (4) and (5) in the main text). In our application, we take $k(\cdot, \cdot)$ to be the isotropic radial basis function,

$$k(\mathbf{v}, \mathbf{v}') = \tau^2 \exp(-\psi \|\mathbf{v} - \mathbf{v}'\|_2^\nu), \quad \tau^2, \psi > 0, \quad \nu \in (0, 2].$$

Remark 1. Under our prior, $\text{cov}\{\mu(\mathbf{v}_h), \mu(\mathbf{v}_s)\} = k(\mathbf{v}_h, \mathbf{v}_s)$ for any pair of $\mathbf{v}_h \in B_h$ and $\mathbf{v}_s \in B_s$.

Proof. Notationally, it is most convenient to show this relationship when $w(\mathbf{v}) = K(B_h, B_h)^{-1}k(B_h, \mathbf{v})$ exactly, though the method is still valid given our approximation in section 2.2, equation (7). Per the definition of $K(\cdot, \cdot)$,

$$\begin{aligned} \text{cov}\{\mu(\mathbf{v}_h), \mu(\mathbf{v}_s)\} &= w^\top(\mathbf{v}_h)k(B_h, \mathbf{v}_s) \\ &= k^\top(B_h, \mathbf{v}_h)K(B_h, B_h)^{-1}k(B_h, \mathbf{v}_s). \end{aligned}$$

Let $\mathbf{d} = [\mathbb{1}(\mathbf{v}_i = \mathbf{v}_h)]_{\mathbf{v}_i \in B_h}$. Since $K(B_h, B_h)\mathbf{d} = k(B_h, \mathbf{v}_h)$ by definition, it follows that,

$$\begin{aligned} k^\top(B_h, \mathbf{v}_h)K(B_h, B_h)^{-1}k(B_h, \mathbf{v}_s) &= \mathbf{d}^\top k(B_h, \mathbf{v}_s) \\ &= k(\mathbf{v}_h, \mathbf{v}_s). \end{aligned}$$

□

References

- ARCHIP, N., CLATZ, O., WHALEN, S., KACHER, D., FEDOROV, A., KOT, A., CHRISOCHOIDES, N., JOLESZ, F., GOLBY, A., BLACK, P. M. et al. (2007). Non-rigid alignment of pre-operative MRI, fMRI, and DT-MRI with intra-operative MRI for enhanced visualization and navigation in image-guided neurosurgery. *NeuroImage* **35** 609–624.
- BANERJEE, S., GELFAND, A. E., FINLEY, A. O. and SANG, H. (2008). Gaussian predictive process models for large spatial data sets. *Journal of the Royal Statistical Society: Series B (Statistical Methodology)* **70** 825–848.
- BERROCAL, V. J., GELFAND, A. E. and HOLLAND, D. M. (2012). Space-time data fusion under error in computer model output: An application to modeling air quality. *Biometrics* **68** 837–848.

- BERTALANFFY, H., BENES, L., MIYAZAWA, T., ALBERTI, O., SIEGEL, A. M. and SURE, U. (2002). Cerebral cavernomas in the adult. Review of the literature and analysis of 72 surgically treated patients. *Neurosurgical review* **25** 1–53.
- BODURKA, J., YE, F., PETRIDOU, N., MURPHY, K. and BANDETTINI, P. A. (2007). Mapping the MRI voxel volume in which thermal noise matches physiological noise—implications for fMRI. *NeuroImage* **34** 542–549.
- BOWMAN, F. D., CAFFO, B., BASSETT, S. S. and KILTS, C. (2008). A Bayesian hierarchical framework for spatial modeling of fMRI data. *NeuroImage* **39** 146–156.
- BOWRING, A., TELSCHOW, F. J., SCHWARTZMAN, A. and NICHOLS, T. E. (2021). Confidence Sets for Cohen’s d effect size images. *NeuroImage* **226** 117477.
- CORDELLA, R., ACERBI, F., BROGGI, M., VAILATI, D., NAZZI, V., SCHIARITI, M., TRINGALI, G., FERROLI, P., FRANZINI, A. and BROGGI, G. (2013). Intraoperative neurophysiological monitoring of the cortico-spinal tract in image-guided mini-invasive neurosurgery. *Clinical Neurophysiology* **124** 1244–1254.
- COX, R., ASHBURNER, J., BREMAN, H., FISELL, K., HASELGROVE, C., HOLMES, C., LANCASTER, J., REX, D., SMITH, S., WOODWARD, J. et al. (2004). A (Sort of) new image data format standard: NIFTI-1: WE 150. *NeuroImage* **22**.
- CRESSIE, N. and GLONEK, G. (1984). Median based covariogram estimators reduce bias. *Statistics & Probability Letters* **2** 299–304.
- DATTA, A., BANERJEE, S., FINLEY, A. O. and GELFAND, A. E. (2016). Hierarchical nearest-neighbor Gaussian process models for large geostatistical datasets. *Journal of the American Statistical Association* **111** 800–812.
- DIGGLE, P. J. (1981). Binary mosaics and the spatial pattern of heather. *Biometrics* 531–539.
- DURNEZ, J., MOERKERKE, B., BARTSCH, A. and NICHOLS, T. E. (2013). Alternative-based thresholding with application to presurgical fMRI. *Cognitive, Affective, & Behavioral Neuroscience* **13** 703–713.
- FESSLER, J. A. and BOOTH, S. D. (1999). Conjugate-gradient preconditioning methods for shift-variant PET image reconstruction. *IEEE Transactions on Image Processing* **8** 688–699.
- FINLEY, A. O., DATTA, A., COOK, B. D., MORTON, D. C., ANDERSEN, H. E. and BANERJEE, S. (2019). Efficient algorithms for Bayesian nearest neighbor Gaussian processes. *Journal of Computational and Graphical Statistics* **28** 401–414.
- FRIGO, M. and JOHNSON, S. G. (2005). The Design and Implementation of FFTW3. *Proceedings of the IEEE* **93** 216–231. Special issue on “Program Generation, Optimization, and Platform Adaptation”.
- FUENTES, M. and RAFTERY, A. E. (2005). Model evaluation and spatial interpolation by Bayesian combination of observations with outputs from numerical models. *Biometrics* **61** 36–45.
- GELFAND, A. E., ZHU, L. and CARLIN, B. P. (2001). On the change of support problem for spatio-temporal data. *Biostatistics* **2** 31–45.
- GELMAN, A., RUBIN, D. B. et al. (1992). Inference from iterative simulation using multiple sequences. *Statistical Science* **7** 457–472.
- GENOVESE, C. R., LAZAR, N. A. and NICHOLS, T. (2002). Thresholding of statistical maps in functional neuroimaging using the false discovery rate. *NeuroImage* **15** 870–878.
- GIROLAMI, M. and CALDERHEAD, B. (2011). Riemann manifold langevin and hamiltonian monte carlo methods. *Journal of the Royal Statistical Society: Series B (Statistical Methodology)* **73** 123–214.
- GROVES, A. R., CHAPPELL, M. A. and WOOLRICH, M. W. (2009). Combined spatial and non-spatial prior for inference on MRI time-series. *NeuroImage* **45** 795–809.
- GUENNEBAUD, G., JACOB, B. et al. (2010). Eigen v3. <http://eigen.tuxfamily.org>.
- HALLER, S. and BARTSCH, A. J. (2009). Pitfalls in fMRI. *European radiology* **19** 2689–2706.
- HOFFMAN, M. D. and GELMAN, A. (2014). The No-U-Turn sampler: adaptively setting path lengths in Hamiltonian Monte Carlo. *Journal of Machine Learning Research* **15** 1593–1623.

- JENKINSON, M., BECKMANN, C. F., BEHRENS, T. E., WOOLRICH, M. W. and SMITH, S. M. (2012). Fsl. *NeuroImage* **62** 782–790.
- JOHNSON, S. G. The NLOpt nonlinear optimization package <http://github.com/stevengj/nlopt>.
- JOVČEVSKA, I., KOČEVAR, N. and KOMEL, R. (2013). Glioma and glioblastoma-how much do we (not) know? *Molecular and clinical oncology* **1** 935–941.
- KAHAN, W. (1965). Pracniques: further remarks on reducing truncation errors. *Communications of the ACM* **8** 40.
- LARGE, I., BRIDGE, H., AHMED, B., CLARE, S., KOLASINSKI, J., LAM, W., MILLER, K., DYRBY, T. B., PARKER, A., SMITH, J. et al. (2016). Individual differences in the alignment of structural and functional markers of the V5/MT complex in primates. *Cerebral Cortex* **26** 3928–3944.
- LINDQUIST, M. A., LOH, J. M. and YUE, Y. R. (2010). Adaptive spatial smoothing of fMRI images. *Statistics and its Interface* **3** 3–13.
- LIU, Z., BERROCAL, V. J., BARTSCH, A. J. and JOHNSON, T. D. (2016). Pre-surgical fMRI data analysis using a spatially adaptive conditionally autoregressive model. *Bayesian Analysis (Online)* **11** 599.
- LIU, Z., BARTSCH, A. J., BERROCAL, V. J. and JOHNSON, T. D. (2019). A mixed-effects, spatially varying coefficients model with application to multi-resolution functional magnetic resonance imaging data. *Statistical Methods in Medical Research* **28** 1203–1215.
- MARDIA, K. V. and MARSHALL, R. J. (1984). Maximum likelihood estimation of models for residual covariance in spatial regression. *Biometrika* **71** 135–146.
- MÜLLER, P., PARMIGIANI, G. and RICE, K. (2006). FDR and Bayesian multiple comparisons rules.
- NEAL, R. M. (2011). MCMC using Hamiltonian dynamics. *Handbook of Markov Chain Monte Carlo* **2** 2.
- NIMSKY, C., GANSLANDT, O., BUCHFELDER, M. and FAHLBUSCH, R. (2006). Intraoperative visualization for resection of gliomas: the role of functional neuronavigation and intraoperative 1.5 T MRI. *Neurological Research* **28** 482–487.
- PENNY, W. D., TRUJILLO-BARRETO, N. J. and FRISTON, K. J. (2005). Bayesian fMRI time series analysis with spatial priors. *NeuroImage* **24** 350–362.
- POWELL, M. J. (1994). A direct search optimization method that models the objective and constraint functions by linear interpolation. In *Advances in Optimization and Numerical Analysis* 51–67. Springer.
- RASMUSSEN, C. E. and WILLIAMS, C. K. (2006). *Gaussian Processes for Machine Learning* **2**. MIT press Cambridge, MA.
- REUTER, M., ROSAS, H. D. and FISCHL, B. (2010). Highly accurate inverse consistent registration: a robust approach. *NeuroImage* **53** 1181–1196.
- RUE, H. and HELD, L. (2005). *Gaussian Markov Random Fields: Theory and Applications*. Chapman and Hall/CRC.
- SEEGER, M., WILLIAMS, C. and LAWRENCE, N. (2003). Fast forward selection to speed up sparse Gaussian process regression Technical Report.
- SIDÉN, P., EKLUND, A., BOLIN, D. and VILLANI, M. (2017). Fast Bayesian whole-brain fMRI analysis with spatial 3D priors. *NeuroImage* **146** 211–225.
- SILVA, M. A., SEE, A. P., ESSAYED, W. I., GOLBY, A. J. and TIE, Y. (2018). Challenges and techniques for presurgical brain mapping with functional MRI. *NeuroImage: Clinical* **17** 794–803.
- STEIN, M. (1999). Interpolation of spatial data. Springer series in statistics.
- STEIN, M. L. et al. (2007). Spatial variation of total column ozone on a global scale. *The Annals of Applied Statistics* **1** 191–210.
- STIPPICH, C. (2015). *Clinical Functional MRI: Presurgical Functional Neuroimaging*. Springer.
- VAN HORN, J. D. and TOGA, A. W. (2009). Multi-site neuroimaging trials. *Current Opinion in*

- Neurology* **22** 370.
- WHITEMAN, A. S. (2022). Source Code Companion to “Bayesian Inference for Brain Activity from Functional Magnetic Resonance Imaging Collected at Two Spatial Resolutions”.
- WHITEMAN, A. S., BARTSCH, A. J., KANG, J. and JOHNSON, T. D. (2022). Supplement to “Bayesian Inference for Brain Activity from Functional Magnetic Resonance Imaging Collected at Two Spatial Resolutions”.
- WOOD, A. T. and CHAN, G. (1994). Simulation of stationary Gaussian processes in $[0, 1]$ d. *Journal of Computational and Graphical Statistics* **3** 409–432.
- WOOLRICH, M. W., RIPLEY, B. D., BRADY, M. and SMITH, S. M. (2001). Temporal autocorrelation in univariate linear modeling of fMRI data. *NeuroImage* **14** 1370–1386.
- WOOLRICH, M. W., JENKINSON, M., BRADY, J. M. and SMITH, S. M. (2004). Fully Bayesian spatio-temporal modeling of fMRI data. *IEEE transactions on medical imaging* **23** 213–231.
- ZHANG, H. (2004). Inconsistent estimation and asymptotically equal interpolations in model-based geostatistics. *Journal of the American Statistical Association* **99** 250–261.
- ZHANG, Y., BRADY, M. and SMITH, S. (2001). Segmentation of brain MR images through a hidden Markov random field model and the expectation-maximization algorithm. *IEEE transactions on medical imaging* **20** 45–57.